Modeling and Decoupled Control of a Buck–Boost and Stacked Dual Half-Bridge Integrated Bidirectional DC–DC Converter

Haixu Shi, *Student Member, IEEE*, Xi Xiao, *Member, IEEE*, Hongfei Wu, *Member, IEEE*, and Kai Sun, *Senior Member, IEEE*

***Abstract*—The modeling and control of a buck–boost and stacked dual half-bridge (DHB) integrated bidirectional dc–dc converter have been studied in this paper. This converter features high-voltage transfer ratio, high efficiency, and the minimum number of switches. In this paper, an extended, continuous, full-order, state-space averaging modeling method is proposed. Compared with existing methods, the proposed method exhibits higher coincidence with the switching circuit simulation, in steady and especially dynamic states. Due to its high dynamic accuracy and low complexity, the proposed modeling method provides a better theoretical analysis and a fast simulation tool for transient process and control design of converters with dual-active-bridge units, especially with DHB units. By using this method, the high-frequency transformer series inductance current is directly divided into a sampled dc component and a fluctuant component. Only the sampled dc one is included into state variables, but both components are considered into state equations. Besides, this method regards the entire converter as a linear superposition of its subsections, which provides a stepwise modeling based on linearization of subsections. Moreover, a decoupled proportional-integral control method is proposed to enhance the stability and dynamic response of the converter. This control method is analyzed by the proposed models, which can be regarded as an application of the proposed modeling method. Simulation and experiments have validated both the proposed modeling and the decoupled control strategy.**

***Index Terms*—DC–DC converters, decoupled control, modeling, transformer series current.**

I. Introduction

BATTERY energy storage systems (BESSs) have attracted much more attention than in the past, since they can be applied to smooth the power output of renewable energy generation systems with an intermittent nature and to increase the penetration of renewable generation. Bidirectional dc–dc converters are key elements in a BESS. They connect the batteries and the high-voltage dc bus and transfer charging/discharging power. High and wide voltage transfer ratio, flexible bidirectional power flow ability, and high efficiency of BDCs are desired [1].

A buck–boost BDC is the simplest BDC, but it suffers from a limited voltage ratio [2]. Multilevel-based BDCs feature reduced voltage stresses and high-voltage transfer ratio, but the switching device cost is high and the voltage balance increases the control complexity [3]. Switched-capacitor converters have been proposed in [4]–[7]. They decrease the voltage stress of devices and need no magnetic component. Switches, however, suffer high transient currents. Coupled-inductance-based BDCs [8] feature high-voltage transfer ratio, but problems associated with leakage inductance create considerable cost. A soft-switched boost converter [9] with an interleaved configuration needs no coupled inductances or switched capacitors, but its output-series structure causes most of the power to be delivered through many diodes, which decreases efficiency. Dual-active-bridge (DAB) BDCs [10] are more attractive for their excellent high-power density and soft-switching performance, but they require the voltages on primary and secondary sides of the transformer matching the transformer ratio. If it fails, the root-mean-square value of transformer series inductance current will increase dramatically due to circulating currents, which leads to higher conduction loss, higher current rating of components, and reduced conversion efficiency. Nevertheless, this requirement is hard to be guaranteed in a BESS. Since the voltage is constant on the high-voltage dc bus side, but on the low-voltage battery side, the voltage varies with the state-of-charge of a battery.

Based on DABs, more advanced high step-up/step-down soft-switching BDCs are proposed. In [11], a converter combining a buck–boost BDC and a dual-half-bridge (DHB) is proposed. It shows that a scheme of a nonisolated pulse width modulation (PWM) converter plus an isolated converter can be a good solution to the mismatched-voltage problem in DABs, since a simple nonisolated PWM converter converts the various battery voltages to a constant.

Based on the work in [11], a buck–boost and stacked DHB integrated bidirectional dc–dc converter (BB-SDHB BDC) is proposed in [12]. The studied BB-SDHB BDC in this paper

Manuscript received November 8, 2016; revised April 19, 2017 and April 24, 2017; accepted May 6, 2017. Date of publication May 19, 2017; date of current version January 3, 2018. This work was supported in part by the National Natural Science Foundation of China (51577102, 51407092), in part by the State Key Lab of Power Systems, Tsinghua University (SKLD15KZ01, SKLD15M07), and in part by the Tsinghua University Initiative Scientific Research Program (20161080044). Recommended for publication by Associate Editor M. Amirabadi. *(Corresponding Author: Kai Sun.)*

H. Shi, X. Xiao, and K. Sun are with the State Key Lab of Power Systems, Tsinghua University, Beijing 100084, China (email: shihaixv666@163.com; xiao_xi@mail.tsinghua.edu.cn; sun-kai@mail.tsinghua.edu.cn).

H. Wu is with the Center for More-Electric-Aircraft Power System, College of Automation Engineering, Nanjing University of Aeronautics and Astronautics, Nanjing 210016, China (e-mail: wuhongfei@nuaa.edu.cn).

Digital Object Identifier 10.1109/TPEL.2017.2705131

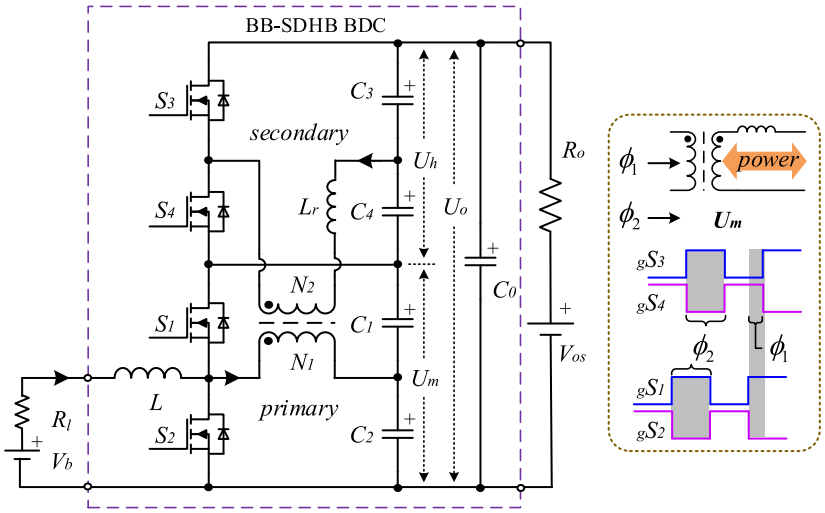

Fig. 1. Topology of BB-SDHB BDC.

is the original type of that in [12], and they are essentially the same. This converter features higher voltage conversion ratio and efficiency. However, the topology of this converter is quite coupled and complex, the modeling and control of this converter has not been discussed. The BB-SDHB BDC is a combination of a buck–boost converter and a stacked DHB converter, as in Fig. 1. Symbols are defined as follows: low electromotive force of storage component V_b and a branch resistance R_l, buck–boost inductor L, power switches S_1, S_2, S_3, S_4, primary and secondary winding numbers of the high-frequency transformer N_1 and N_2 ($N_1 < N_2$), series inductor L_r, switching capacitors C_1, C_2, C_3, C_4 and their voltages v_1, v_2, v_3, v_4, high-voltage side capacitor C_0, high-voltage branch resistance R_o, and high-voltage source V_{os}. Intermediate voltage U_m equals $v_1 + v_2$. Secondary-side bus voltage U_h equals $v_3 + v_4$. High-voltage side bus voltage U_o equals $U_m + U_o$. PWM period of all switches is T_s. Duty cycles of all power switches are D (D $= \phi_2/2\pi$ and ϕ_2 takes place of D in this paper for facilitating analysis). Drives of $S_{1\sim2}$ are compensatory ${}_gS_{1\sim2}$, similarly for $S_{3\sim4}$. Shifted phase between carriers of ${}_gS_{1\sim2}$ and ${}_gS_{3\sim4}$ is ϕ_1. Range for ϕ_1 and ϕ_2 is: $\phi_2 \in [0, 2\pi]$, $\phi_1 \in [-0.5\min(\phi_2, 2\pi - \phi_2), 0.5\min(\phi_2, 2\pi - \phi_2)]$.

For modeling, conventional state-space averaging modeling is generally utilized for its linearization in the sense of a state average without switching details during a PWM cycle [14]. Nevertheless, it is difficult to deal with the series inductance current of a high-frequency transformer in a DAB converter unit such as in the studied converter, since its average of a PWM cycle is mostly zero. The series inductance is a main power transfer element in this converter. Its current may create oscillations in transients and unbalance the voltages of switching capacitors. Therefore, this state should be cautiously considered in modeling. Facing this challenge, scholars have developed some modeling methods, but room for improvement still exists. In [15]–[17], reduced order models are obtained. The series inductance current is eliminated from the state space by assuming its current cycle average is always zero. Its ac wave is derived by voltages on the primary and secondary sides of the transformer. These methods are good solutions, but are restricted owing to a 50% duty cycle. In addition, information and the influence of the average value in dynamics are lost. Similar methods, along with duty cycle modulation for reduced order models, were developed and described in [18] and [19]. In these methods, a constant is utilized to represent PWM cycle initial current value instead of the zero-average concept, since its main issue is a small signal modeling. In [20], a discrete full-order model with the first term of a Taylor expansion is developed, but the information of higher degree terms is lost. In [21] and [22], the second terms of a Fourier series are introduced into the current for more accuracy, but the first dc, second sine, and cosine terms divide the current into three states, which increases the complexity. Moreover, the information of higher degree terms is lost as well. Since the cycle average of this current is mainly not zero in dynamics, in [23] an improvement was made; namely, that the average of this current in a PWM cycle is included into state variables to obtain a full-order continuous model. However, in a PWM cycle, the current average value and current detailed waves are mutually determined, which causes a trouble in derivation of the average value. This problem is discussed in Section III-E.

For control, as the working principle of BB-SDHB BDC in Section II and Fig. 1, U_m is regulated by ϕ_2 through the buck–boost unit, which is constructed by L, S_1, S_2, C_1, and C_2. The power delivered by the transformer between $C_{1\sim2}$ (U_m) and $C_{3\sim4}$ (U_h) is regulated by ϕ_1 through the SDHB unit, which is constructed by the transformer, L_r, $S_{1\sim4}$, and $C_{1\sim4}$. In the early stage of our experiment, when supplying R_o with $V_{os} = 0$ V under the boost mode, two proportional-integral (PI) controllers were used to control U_m and U_o. The control variable of the U_o loop is ϕ_1 [15], while that of the U_m loop is ϕ_2. Since $U_o = U_m + U_h$, U_o is influenced by both ϕ_1 and ϕ_2, hence it is referred as "coupled control strategy" in this paper. Our previous experiments show that the oscillation easily occurs under this "coupled control strategy," as shown in Fig. 18. This

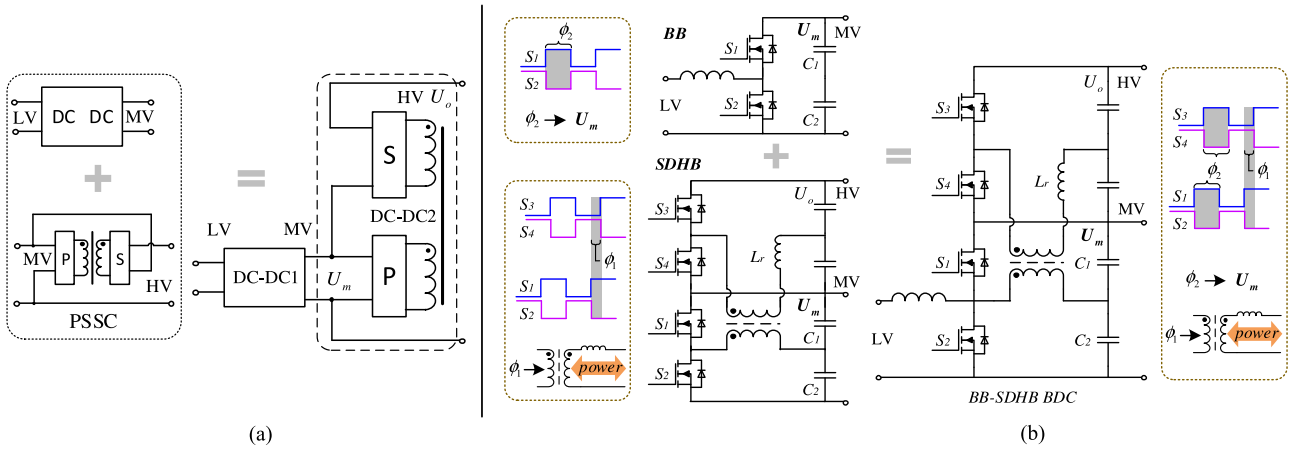

Fig. 2. Derivation of topology: (a) VM-SDCT BDC and (b) BB-SDHB BDC.

phenomenon aroused our curiosity to study modeling and control of this converter.

The major works of this paper are: 1) an extended, continuous, full order, state-space averaging modeling method is proposed. Compared with existing methods, the proposed one features higher coincidence with the switching circuit simulation, in steady and especially dynamic states. Due to its high dynamic accuracy and low complexity, the proposed modeling method provides a better theoretical analysis and fast simulation tool for transient process and control design of converters with DAB units, especially with DHB units. By using this method, the high-frequency transformer series inductance current is directly divided into a sampled dc component and a fluctuant component. This fluctuant component can be represented completely by switching capacitor voltages, duty cycle phase, and shifted phase. Hence, only the sampled dc component is included into state variables. But both components are considered into state equations of switching capacitor voltages (other state variables). Besides, this method regards the entire converter as a linear superposition of its subsections, which provides a stepwise modeling based on linearization of subsections. In particular, the average value of this current in a PWM cycle is deftly avoided being used in specific modeling, since the current direct division concept is utilized to model this current instead of the average value concept. This current division concept solves the problem in [23] that the average value is difficult to obtain. And it features lower algebraic degree (2 instead of 3) of expressions of duty cycle and shifted phase in the model, which benefits for lowering model complexity. 2) A "decoupled control strategy" is proposed to achieve better control performance of BB-SDHB BDC and the topological family that it belongs to. This control strategy is analyzed based on the established model, which is also an application of the proposed modeling method.

In Section II, the converter and the topological family it belongs to are introduced. In Section III, both large- and small-signal models are established with the proposed modeling method. The two models are verified by the switching circuit simulation. The proposed modeling method is also compared with a zero-average current method based on [15], and an average-current state method [23]. In Section IV, the "decoupled control strategy" is compared with the "coupled control strategy." In Section V, both proposed modeling and control are verified by an experiment.

II. Topology and Operational Principles

The studied converter BB-SDHB BDC in this paper is shown in Fig. 1. To understand the working principle of this converter, DAB BDCs should be concerned first. A shifted-phase DAB BDC is an attractive solution for energy storage systems, but it requires the voltages on two side buses of the transformer keeping matched. In addition, the conversion efficiency is reduced since all power has to be transferred through the transformer. An idea to deal with the problem of voltage mismatch is cascading a simple nonisolated dc–dc converter, such as a buck–boost circuit, to the low-voltage battery side, so as to keep the voltage a proper constant on the low-voltage side of the DAB part. An idea to deal with the problem of efficiency is a stacking structure (primary and secondary bus series connected PSSC) such as that shown in Fig. 2(a). It is obvious that not all power needs to be transferred, which benefits efficiency. The voltage conversion ratio also becomes higher due to the stacking of primary and secondary dc buses. Hence, a scheme that integrates the two units can be derived as shown in Fig. 2 (a). This converter family can be designated voltage matcher and stacked dc-transformer integrated bidirectional dc–dc converters (VM-SDCT BDCs). The BB-SDHB BDC studied in this paper and is a typical example of the family. Its topology derivation is shown in Fig. 2(b). This converter comes from an isolated type [11] and has the following advantages [11]: 1) DHB converters need the minimum switches in DAB converters. 2) This converter couples the boost circuit and primary bridge based on switch reuse, which further reduces switch numbers and conversion stages to reduce cost and enhance efficiency.

The VM-SDCT BDCs have two working modes. In buck mode, power flows from the high-voltage (HV) side to the low-voltage (LV) side that is usually connected to an energy storage component such as a battery or supercapacitor, while in boost mode the power flow is reversed. U_m is regulated by DC–DC1. Thus, while the LV side voltage varies, the voltages of both

transformer sides in DC–DC2 can remain matched under certain control for power density and efficiency. The power delivered by the transformer is regulated by DC–DC2 with phase shift control, which is similar to DAB converters. These two modes smoothly transition to each other with the shifted phase slowly changing to the opposite sign.

The studied converter BB-SDHB BDC works similarly, as in the dashed box of Fig. 2(b). U_m is regulated by the coupled buck–boost unit (DC–DC1) through ϕ_2. The power delivered by transformer between $C_{1\sim2}$ and $C_{3\sim4}$ is regulated by the SDHB (DC–DC2) through ϕ_1. The detailed operating principle is similar to that in [12]. Average power transferred in the steady state is shown in

$$P_{av} = \frac{T_s N_1 V_b U_o \phi_1}{2\pi N_2 L_r}\left(1 - \frac{\phi_2}{2\pi} - \frac{\phi_1}{2\phi_2}\right). \tag{1}$$

For BB-SDHB BDC, as shown in Fig. 1, the LV side connects low-voltage dc bus of the storage components that can be emulated by a series of a resistance R_l and a voltage source V_b. The HV load and HV dc bus can be emulated by a series of a resistance R_o and a voltage source V_{os}. When the converter supplies R_o on the HV side, R_o is relatively large and V_{os} is zero, while when the HV side is connected to a dc grid, R_o is relatively small and V_{os} is high. While on the LV side, R_l is always a small value including L resistance, inner resistance of V_b, and on-state resistance of switches. The inner resistance of V_b plays a major role, and if it accounts for almost all of R_l, R_l can be set as its value. V_b is always the voltage of the storage component.

III. Modeling and Analysis

A. Core Ideas of Modeling

Before modeling, the following assumptions are made: the ideal transformer has series inductance, the magnetizing inductance is ignored since it is very large, there are no distributed parameters, and the switch, passive component, and voltage source are ideal.

1) Transformer Series Inductance Current: The proposed modeling method straightforwardly converts the series inductance current i_{Lr} into a dc state variable in a sense. The simplified transformer model is shown in Fig. 3(a). i_{Lr} rises, falls, and shares the same period with PWM cycle. V_{Lr1} and V_{Lr2} are port voltages converted to the secondary side.

As shown in Fig. 3(b), sampling i_{Lr} at one same time point of each PWM cycle, a "dc" quantity of i_{Lr} can be observed. For convenience, i_{Lr} is sampled at the beginning of each cycle. Thus, in each PWM cycle, i_{Lr} can be divided into two components: one is this sampled component i_{Lr0}(i_{Lr0} does not vary during a whole cycle), while the other is a fluctuant component i_{LrFl}. There is always an (2) at any time

$$i_{Lr} = i_{Lr0} + i_{LrFl}. \tag{2}$$

The symbols $i_{LrFl}^{[n]}$, $i_{Lr0}^{[n]}$ represent the values of i_{LrFl}, i_{Lr0} in cycle$^{[n]}$. And $i_{LrFl}^{[n+1]}$, $i_{Lr0}^{[n+1]}$ represent the values of i_{LrFl}, i_{Lr0} in next cycle (cycle$^{[n+1]}$). Thus, i_{Lr0} can be modeled using a conventional state-space averaging method as in (3). Where T_s is the period of a cycle, ω is the phase velocity, $\omega T_s = 2\pi$, t is the time, and $\dot{i}_{Lr0}$ is the state averaging change rate of i_{Lr0} in cycle$^{[n]}$

$$\dot{i}_{Lr0} = \frac{i_{Lr0}^{[n+1]} - i_{Lr0}^{[n]}}{T_s} = \frac{1}{T_s}\int_0^{T_s} \frac{V_{Lr1} - V_{Lr2}}{L_r} dt. \tag{3}$$

Fig. 3(c) shows i_{Lr0} and i_{LrFl}, respectively, to help illustrate this division. Owing to (2) and i_{Lr0} sampled at the beginning of each cycle, $i_{LrFl}^{[n]}$ is zero at the beginning of cycle$^{[n]}$. The fluctuation of $i_{LrFl}^{[n]}$ is determined by $V_{Lr1} - V_{Lr2}$, as in (4), where $\dot{i}_{LrFl}$ is the instant change rate of i_{LrFl}

$$\begin{cases} \dot{i}_{LrFl} = \dfrac{V_{Lr1} - V_{Lr2}}{L_r} \\ i_{LrFl}^{[n]}|_{\omega t=0} = 0 \end{cases}. \tag{4}$$

Obviously, $V_{Lr1} - V_{Lr2}$ can be determined by t, switching capacitor voltages $v_{\mathrm{p}1}, v_{\mathrm{p}2}, v_{\mathrm{s}1}, v_{\mathrm{s}2}$, and ϕ_1, ϕ_2

$$V_{Lr1} - V_{Lr2} = \begin{cases} v_{\mathrm{p}1} - v_{\mathrm{s}2}, 0 \le \omega t < \phi_1 \\ v_{\mathrm{p}1} - v_{\mathrm{s}1}, \phi_1 \le \omega t < \phi_2 \\ v_{\mathrm{p}2} - v_{\mathrm{s}1}, \phi_2 \le \omega t < \phi_1 + \phi_2 \\ v_{\mathrm{p}2} - v_{\mathrm{s}2}, \phi_1 + \phi_2 \le \omega t < 2\pi \end{cases}. \tag{5}$$

Combining (3) and (5), $i_{Lr0}^{[n+1]}$ can be derived as a function f_0 of $i_{Lr0}^{[n]}$, $\phi_{1\sim2}$, $v_{\mathrm{p}1\sim2}$, $v_{\mathrm{s}1\sim2}$

$$i_{Lr0}^{[n+1]} = f_0(i_{Lr0}^{[n]}, \phi_{1\sim2}, v_{\mathrm{p}1\sim2}, v_{\mathrm{s}1\sim2}). \tag{6}$$

Combining (4) and (5), $i_{LrFl}^{[n+1]}$ can be derived as a function f_{Fl} of t, $\phi_{1\sim2}$, $v_{\mathrm{p}1\sim2}$, $v_{\mathrm{s}1\sim2}$

$$i_{LrFl}^{[n]} = f_{Fl}(t, \phi_{1\sim2}, v_{\mathrm{p}1\sim2}, v_{\mathrm{s}1\sim2}). \tag{7}$$

From (6) and (7), it is shown that $i_{Lr0}^{[n+1]}$ depends on $i_{Lr0}^{[n]}$, while $i_{LrFl}^{[n]}$ is independent of $i_{LrFl}^{[n-1]}$. Thus, i_{Lr0} should be a state variable, while i_{LrFl} is not a state variable. Thus, i_{Lr} occupies only one order in the model. i_{Lr0} and i_{LrFl} are modeled by (6) and (7), respectively. Equations (9) and (10) are modeling results of i_{LrFl} and i_{Lr0} for the studied converter. The detailed modeling procedure is presented in Section III.

It is important to notice that average of $i_{LrFl}^{[n]}$ in cycle$^{[n]}$ is not necessarily zero, i_{LrFl} is not a conventional "ac" component, but a fluctuant component. Another attention is that the end value of $i_{LrFl}^{[n]}$ is also not necessarily zero, because $V_{Lr1} - V_{Lr2}$ during cycle$^{[n]}$ may not make $i_{LrFl}^{[n]}$ zero at the end. But owing to definition, $i_{LrFl}^{[n+1]}$ is zero at the beginning of cycle$^{[n+1]}$ (end of cycle$^{[n]}$), which means that i_{LrFl} does not need to be continuous at the boundary of two adjacent cycles, as in Fig. 3(c). i_{Lr0} is also discrete at the boundary apparently. But $i_{Lr} = i_{Lr0} + i_{LrFl}$ is continuous at any time, which ensures all information of i_{Lr} is conserved. Universality of this current division and full information of the current wave are the key points to ensure high accuracy of the proposed modeling method.

Both i_{LrFl} and i_{Lr0} contribute to the power transfer. And their contribution is fully derived into the state equations of switching capacitor voltages $v_{\mathrm{p}1\sim2}, v_{\mathrm{s}1\sim2}$ (other state variables). But since

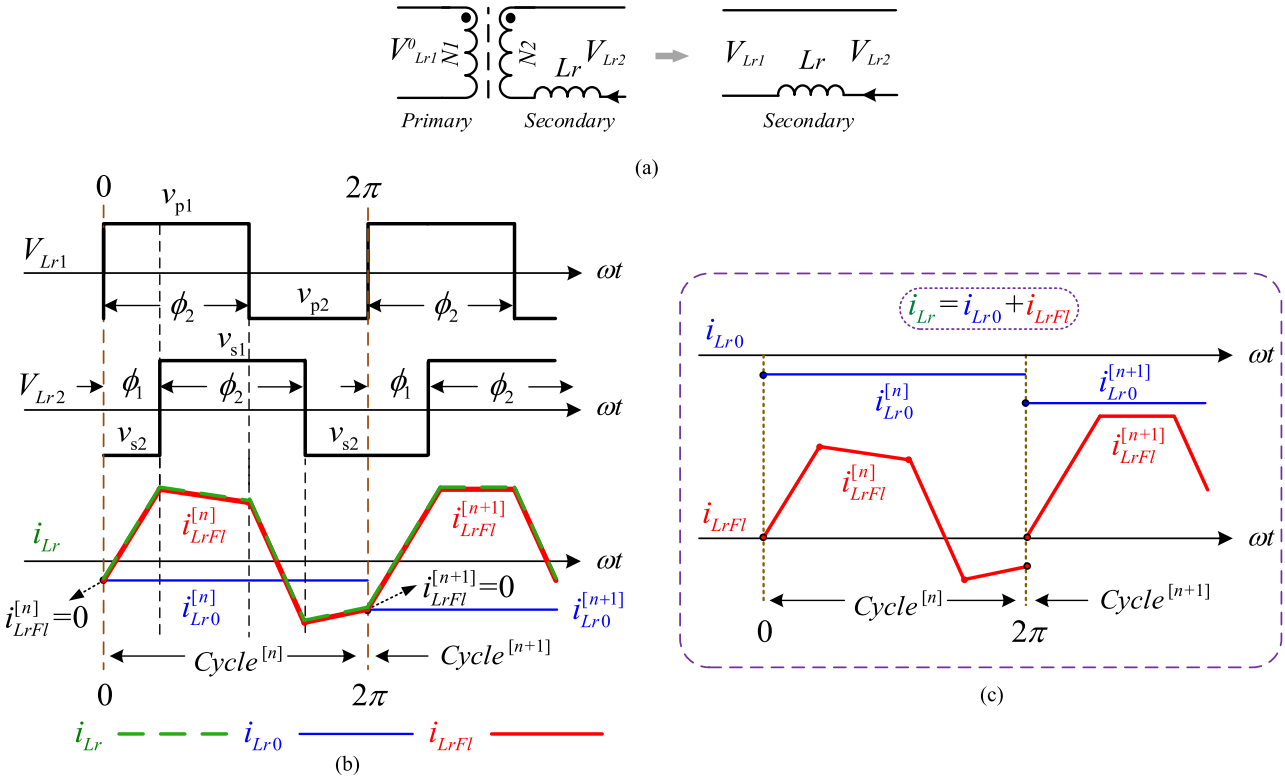

Fig. 3. Operation modes of dual-bridge converter: (a) simplified transformer, (b) division of transformer series inductance current, and (c) two components from division.

i_{LrFl} is not a state variable, only its contribution is incorporated in final state equations, while "i_{LrFl}" does not appear in the state equation. The detailed derivation process is presented in Section III-B.

2) Capacitor Voltages: An average-charge method is proposed to analyze the variation of capacitor voltages. This method is a part of the entire modeling method proposed in this paper. It is still based on state-space averaging, but much easier to execute and analyze than averaging all of the switching state equations, due to the complex coupling of the converter. The core idea is to divide the converter into subsections by their function. The capacitor voltages are kept nearly constant in a PWM cycle, thus the contribution of each subsection to the charge of a capacitor can be calculated in the sense of state averaging. Then, charge of each capacitor is linear superposition of contribution from these subsections. Finally, the entire model is established. For instance, the selected converter is the combination of a buck–boost unit, SDHB unit, and load branch loop.

B. Large -Signal Modeling Procedure

For the studied converter, the operation modes of one PWM switching cycle are illustrated in Fig. 4.

A PWM cycle is divided into four intervals by time

$$w_0 = \frac{\phi_1}{2\pi}T_s, w_1 = \frac{\phi_2-\phi_1}{2\pi}T_s, w_2 = \frac{\phi_1}{2\pi}T_s, w_3 = \frac{2\pi-\phi_1-\phi_2}{2\pi}T_s. \quad (8)$$

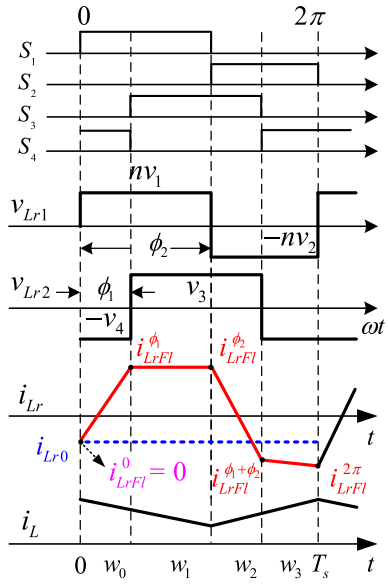

Fig. 4. Operation modes of BB-SDHB BDC.

Only series inductance on the primary side is transferred to the secondary side for analysis, due to the fact that there is no isolation between buses of two sides. In boost mode, the time V_{Lr1} steps up is selected as the sample time of i_{Lr} for i_{Lr0}, and as beginning of a cycle for convenience. While the time V_{Lr2} steps up is selected in buck mode. This selection guarantees that the converter can be modeled with the similar procedure in

both buck and boost mode. As shown in Fig. 4, i^{0}_{LrFl}, $i^{\phi_1}_{LrFl}$, $i^{\phi_2}_{LrFl}$, $i^{\phi_1+\phi_2}_{LrFl}$, $i^{2\pi}_{LrFl}$ are key values of i_{LrFl}, where $i^{0}_{LrFl}=0$. Voltages $[v]=[\,v_1\ v_2\ v_3\ v_4\,]$ of C_1, C_2, C_3 and C_4, L current i_L, and i_{Lr0} are selected to constitute state space.

Key points of i_{LrFl} are derived in (9), shown at the bottom this page, by (4), (5). and (8), where *n* is the transformer ratio defined as N_2/N_1:

Hence, average change rate of i_{Lr0} in a PWM cycle can be derived in (10) by (3), (9), and (8)

$$\begin{aligned}\dot{i}_{Lr0}&=\frac{i^{2\pi}_{LrFl}-i^{0}_{LrFl}}{T_s}=[H_{i_{Lr0}\_v}][v]\\&=\frac{\phi_2 n}{2\pi L_r}v_1-\frac{(2\pi-\phi_2)n}{2\pi L_r}v_2-\frac{\phi_2}{2\pi L_r}v_3+\frac{2\pi-\phi_2}{2\pi L_r}v_4.\end{aligned}\tag{10}$$

By calculating charge with an integral of i_{Lr} in a cycle ($i_{Lr}=i_{Lr0}+i_{LrFl}$), and considering equivalent capacitance, the variations of capacitor voltages caused by i_{Lr} can be acquired. To begin with, during a PWM cycle T_s, while S_1 is on, its current component of SDHB i^{SDHB}_{S1} (i_L component in S_1 is excluded) equals ni_{Lr}. This current flows into an equivalent capacitor as shown in Fig. 5(a). This capacitor is constructed by paralleling C_1 and C_{1N}, where C_{1N} is the series branch of C_2, C_3, C_4, C_0, and C_{1N} can be calculated by $C_{iN}=1/\sum_{j\neq i}^{M=0\sim4}\frac{1}{C_j}$.

The contribution made by i^{SDHB}_{S1} to the change of v_1 in a cycle is represented by $\triangle v_{10}$. It can be derived as (11), shown at the bottom of this page, by (9) and (8):

For the current of S_2, S_3, S_4, corresponding $\triangle v_{20}$, $\triangle v_{30}$, $\triangle v_{40}$ can be derived similarly. Their vector form $[\Delta v_0]=[\,\Delta v_{10}\ \Delta v_{20}\ \Delta v_{30}\ \Delta v_{40}\,]^{\mathrm{T}}$ can be derived as follows:

$$[\Delta v_0]=T_s[M_{Cv0}]([Q_{i_{Lr0}}][\boldsymbol{i}_{Lr0}]+[H_{v0}]\,[\boldsymbol{v}])\tag{12}$$

where

$$[M_{Cv0}]=\begin{bmatrix}\dfrac{-n}{C_{1N}+C_1}&0&0&0\\0&\dfrac{n}{C_{2N}+C_2}&0&0\\0&0&\dfrac{1}{C_{3N}+C_3}&0\\0&0&0&\dfrac{-1}{C_{4N}+C_4}\end{bmatrix},$$

$$[Q_{i_{Lr0}}]=\frac{1}{2\pi}\big[\,\phi_2\ 2\pi-\phi_2\ \phi_2\ 2\pi-\phi_2\,\big]^{\mathrm{T}}$$

and $[H_{v0}]$ is detailed in (14), shown at the bottom of the next page.

When S_1 is on, the current of S_1 also contributes to the changes of v_1, v_2, v_3, v_4 as shown in Fig. 5(a). For v_i ($i\neq1$), this voltage change Δv_{1_i} can be derived by

$$\Delta v_{1\_i}=-\frac{C_{1N}}{C_i}\Delta v_{10}.\tag{13}$$

When S_2, S_3, S_4 are on, respectively, their currents also contribute to the change of v_1; hence, the total variation of v_1 caused by i_{Lr} is shown in (15)

$$\begin{aligned}\Delta v_{iLr\_1}&=\Delta v_{10}+\Delta v_{2\_1}+\Delta v_{3\_1}+\Delta v_{4\_1}\\&=\Delta v_{10}-\frac{C_{2N}}{C_1}\Delta v_{20}-\frac{C_{3N}}{C_1}\Delta v_{30}-\frac{C_{4N}}{C_1}\Delta v_{40}.\end{aligned}\tag{15}$$

Δv_{iLr_2}, Δv_{iLr_3}, Δv_{iLr_4} can be derived similarly. Their vector form $[\triangle v_{iLr}]=[\,\Delta v_{iLr\_1}\ \Delta v_{iLr\_2}\ \Delta v_{iLr\_3}\ \Delta v_{iLr\_4}\,]^{\mathrm{T}}$ is expressed in

$$[\triangle v_{iLr}]=[M_{Cv\_v0}][\triangle v_0]\tag{16}$$

$$\begin{cases}i^{0}_{LrFl}=0\\ i^{\phi_1}_{LrFl}=i^{0}_{LrFl}+\dfrac{w_0(nv_1+v_4)}{L_r}=\dfrac{\phi_1 nv_1+\phi_1 v_4}{2\pi L_r}T_s\\ i^{\phi_2}_{LrFl}=i^{\phi_1}_{LrFl}+\dfrac{w_1(nv_1-v_3)}{L_r}=\dfrac{\phi_2 nv_1-(\phi_2-\phi_1)v_3+\phi_1 v_4}{2\pi L_r}T_s\\ i^{\phi_1+\phi_2}_{LrFl}=i^{\phi_2}_{LrFl}+\dfrac{w_2(nv_2-v_3)}{L_r}=\dfrac{\phi_2 nv_1-\phi_1 nv_2-\phi_2 v_3+\phi_1 v_4}{2\pi L_r}T_s\\ i^{2\pi}_{LrFl}=i^{\phi_1+\phi_2}_{LrFl}+\dfrac{w_3(nv_2+v_4)}{L_r}\\ \qquad=\dfrac{\phi_2 nv_1-(2\pi-\phi_2)nv_2-\phi_2 v_3+(2\pi-\phi_2)v_4}{2\pi L_r}T_s\end{cases}\tag{9}$$

$$\begin{aligned}\Delta v_{10}&=\frac{-n(i_{Lr0}(w_1+w_2)+\frac{1}{2}(i^{0}_{LrFl}+i^{\phi_1}_{LrFl})w_1+\frac{1}{2}(i^{\phi_1}_{LrFl}+i^{\phi_2}_{LrFl})w_2)}{C_{1N}+C_1}\\&=T_s\frac{-n(\frac{\phi_2}{2\pi}\boldsymbol{i}_{Lr0}+\frac{T_s}{8\pi^2 L_r}(n\phi_2^2\boldsymbol{v}_1-(\phi_2-\phi_1)^2\boldsymbol{v}_3+(-\phi_1^2+2\phi_1\phi_2)\boldsymbol{v}_4))}{C_{1N}+C_1}\end{aligned}\tag{11}$$

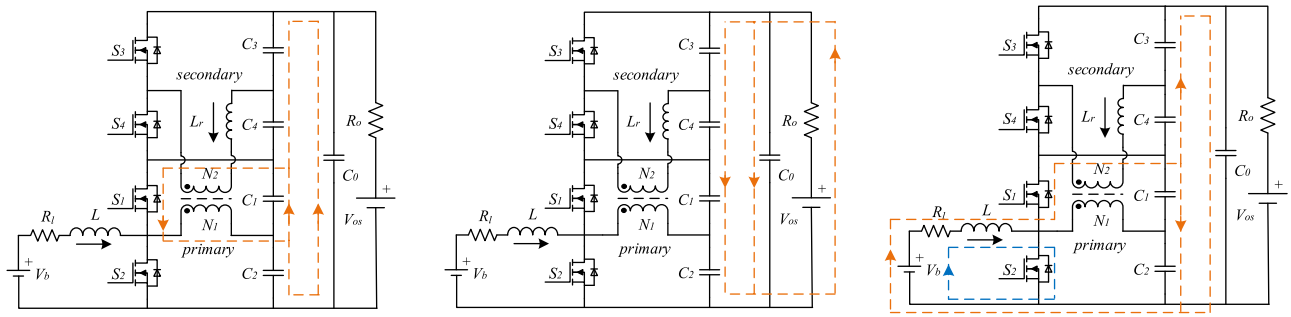

Fig. 5. Some charging processes of different units: (a) S_1 current component of SDHB, (b) R_o current, and (c) L current.

where

$$[M_{Cv\_v0}] = \begin{bmatrix} 1 & -\frac{C_{2N}}{C_1} & -\frac{C_{3N}}{C_1} & -\frac{C_{4N}}{C_1} \\ -\frac{C_{1N}}{C_2} & 1 & -\frac{C_{3N}}{C_2} & -\frac{C_{4N}}{C_2} \\ -\frac{C_{1N}}{C_3} & -\frac{C_{2N}}{C_3} & 1 & -\frac{C_{4N}}{C_3} \\ -\frac{C_{1N}}{C_4} & -\frac{C_{2N}}{C_4} & -\frac{C_{3N}}{C_4} & 1 \end{bmatrix}.$$

Besides i_{Lr}, the coupled buck–boost unit also charges capacitors through S_1 by i_L as shown in Fig. 5(c). Considering the equivalent capacitance, its contribution can be derived as follows:

$$\begin{aligned}[\Delta v_{iL}] &= T_s[H_{v\_i_L}]\,[i_L] \\ &= T_s \frac{\phi_2}{2\pi(C_{Lp}+C_{Ls})} \left[\begin{array}{cccc} \frac{C_{Lp}}{C_1} & \frac{C_{Lp}}{C_2} & \frac{-C_{Ls}}{C_3} & \frac{-C_{Ls}}{C_4} \end{array}\right]^{\mathrm{T}} [i_L] \end{aligned} \tag{17}$$

where

$$C_{Lp} = \frac{C_1C_2}{C_1+C_2}, C_{Ls} = \frac{C_3C_4C_0}{C_3C_4+C_4C_0+C_3C_0}.$$

The current of R_o branch on the HV side charges these capacitors too, as shown in Fig. 5(b), and its contribution can be derived as follows:

$$[\Delta v_{Ro}] = T_s[M_{C\_Ro}](V_{os}-v_1-v_2-v_3-v_4)/R_o \tag{18}$$

where

$$[M_{C\_Ro}] = \frac{C_{0N}}{C_{0N}+C_0}\left[\begin{array}{cccc} \frac{1}{C_1} & \frac{1}{C_2} & \frac{1}{C_3} & \frac{1}{C_4} \end{array}\right]^{\mathrm{T}}.$$

Hence, the total voltage change rate in a cycle is

$$\begin{aligned}[\dot{v}] &= [\Delta v_{iL}] + [\Delta v_{iLr}] + [\Delta v_{Ro}])/T_s \\ &= [H_{v\_i_L}][\boldsymbol{i}_L] + [H_{v\_i_{Lr0}}][\boldsymbol{i}_{Lr0}] + [H_{v\_v}][\boldsymbol{v}] \\ &\quad + [M_{C\_Ro}]V_{os}/R_o \end{aligned} \tag{19}$$

where

$$\begin{aligned}[H_{v\_i_{Lr0}}] &= [M_{Cv\_v0}][M_{Cv0}][Q_{i_{Lr0}}], \\ [H_{v\_v}] &= [M_{Cv\_v0}][M_{Cv0}][H_{v0}] - [M_{Cv\_Ro}]/R_o, \end{aligned}$$

$$[M_{Cv\_Ro}] = \frac{C_{0N}}{C_{0N}+C_0}\begin{bmatrix} \frac{1}{C_1} & \frac{1}{C_1} & \frac{1}{C_1} & \frac{1}{C_1} \\ \frac{1}{C_2} & \frac{1}{C_2} & \frac{1}{C_2} & \frac{1}{C_2} \\ \frac{1}{C_3} & \frac{1}{C_3} & \frac{1}{C_3} & \frac{1}{C_3} \\ \frac{1}{C_4} & \frac{1}{C_4} & \frac{1}{C_4} & \frac{1}{C_4} \end{bmatrix}.$$

The change of i_L can be simply derived by the current flow shown in Fig. 5(c) as follows:

$$\begin{aligned}\dot{i}_L &= -\frac{R_l}{L}i_L - \frac{\phi_2}{2\pi L}v_1 - \frac{\phi_2}{2\pi L}v_2 + \frac{1}{L}V_b \\ &= -\frac{R_l}{L}i_L + [H_{i_L\_v}][v] + \frac{1}{L}V_b. \end{aligned} \tag{20}$$

$$H_{v0} = \frac{T_s}{8\pi^2 L_r}\begin{bmatrix} n\phi_2^2 & 0 & -(\phi_2-\phi_1)^2 & -\phi_1^2+2\phi_1\phi_2 \\ 2n\phi_2(2\pi-\phi_2) & -n(2\pi-\phi_2)^2 & \phi_1^2+2\phi_2^2-4\pi\phi_2 & \phi_1^2+(2\pi-\phi_2)^2 \\ n(-\phi_1^2+2\phi_1\phi_2+\phi_2^2) & -n\phi_1^2 & -\phi_2^2 & 2\phi_1\phi_2 \\ n(\phi_1^2+2\phi_2(2\pi-\phi_1-\phi_2)) & n(\phi_1^2-(2\pi-\phi_2)^2) & -2\phi_2(2\pi-\phi_1-\phi_2) & (2\pi-\phi_2)^2 \end{bmatrix} \tag{14}$$

Finally, combining (20), (10), (19), the entire large-signal model is established as follows:

$$\begin{bmatrix} \dot{i}_L \\ \dot{i}_{Lr0} \\ \dot{v}_1 \\ \dot{v}_2 \\ \dot{v}_3 \\ \dot{v}_4 \end{bmatrix} = \begin{bmatrix} -\dfrac{R_l}{L} & 0 & [H_{i_L\_v}] \\ 0 & 0 & [H_{i_{Lr0}\_v}] \\ [H_{v\_i_L}] & [H_{v\_i_{Lr0}}] & [H_{v\_v}] \end{bmatrix} \begin{bmatrix} i_L \\ i_{Lr0} \\ v_1 \\ v_2 \\ v_3 \\ v_4 \end{bmatrix} + \begin{bmatrix} \dfrac{1}{L} & 0 \\ 0 & 0 \\ [0] & \dfrac{[M_{C\_Ro}]}{R_0} \end{bmatrix} \begin{bmatrix} V_b \\ V_{os} \end{bmatrix}. \quad (21)$$

The detailed large-signal modeling result is presented in Section VIII. Appendix is presented at the end of this paper.

C. Small-Signal Modeling Procedure

ϕ_1 and ϕ_2 are control inputs and cause nonlinearity of the model system. Thus, a small-signal model based on (21) is established for linearization to make analyzing the convertor performance convenient. A good feature is that state variables do not produce nonlinearity.

The state space is represented as $x_0 = [i_L \;\; i_{Lr0} \;\; v_1 \;\; v_2 \;\; v_3 \;\; v_4]^{\mathrm{T}}$, and outputs are $U_m = v_1 + v_2$, $U_h = v_3 + v_4$, $U_o = U_m + U_h$. Thus, the state-space equations can be presented by rewriting (21) into $\dot{x}_0 = G(\phi_1, \phi_2)x_0 + Bv_S$. By introducing small perturbations $\tilde{x}$, $\mathrm{d}\phi_1$, and $\mathrm{d}\phi_2$ to x_0, ϕ_1, and ϕ_2, the small-signal model can be derived as (22), where ${c_m}^T = [\,0\;0\;1\;1\;0\;0\,]$, ${c_o}^T = [\,0\;0\;1\;1\;1\;1\,]$, and ${c_h}^T = [\,0\;0\;0\;0\;1\;1\,]$

$$\begin{cases} \dot{\tilde{x}} \approx G\tilde{x} + (\partial G/\partial\varphi_1)x_0\mathrm{d}\phi_1 + (\partial G/\partial\varphi_2)x_0\mathrm{d}\phi_2 \\ \mathrm{d}U_m = {c_m}^T\tilde{x} \\ \mathrm{d}U_h = {c_h}^T\tilde{x} \\ \mathrm{d}U_o = {c_o}^T\tilde{x} \end{cases}. \quad (22)$$

D. Verification with Circuit Simulation

To test the proposed modeling method, three models were built: a large-signal model based on (21), a small-signal model based on (22), and a detailed switching circuit simulation model. All models are built in MATLAB/Simulink. The former two mathematical models are built by using mathematic modules, and the switching circuit simulation model is built by using electrical elements. System parameters of these models are the same and are from a prototype; they are listed in Table I, where $1/T_s$ is switching frequency, L_{m} is magnetizing inductance, and *n* is the transformer ratio.

1) Large-Signal Model Performance: The performance of the large-signal model is tested under both boost and buck modes, with the results shown in Figs. 6 and 7, respectively, where $V_b = 40$ V,$V_{os} = 0$ V(boost mode)/ 400 V(buck mode), $R_l = 0.01\,\Omega$, $R_o = 326.1\,\Omega$(boost mode)/0.1Ω(buck mode). The initial values are listed in Table II. The step excitations are produced by ϕ_1 and ϕ_2 since they are the control variables.

TABLE I
SIMULATION AND MODEL PARAMETERS

U_{o_rated}	400 V	L_m	∞
U_{m_rated}	100 V	C_0	3.3 μF
L	20 μH	C_1	96 μF
L_{r}	23 μH	C_2	96 μF
$1/T_s$	100 kHz	C_3	6.6 μF
n	3	C_4	6.6 μF

TABLE II
INITIAL CONDITIONS FOR TESTING LARGE-SIGNAL MODEL PERFORMANCE

State variable	i_L	$i_{Lr(0)}$	v_1	v_2	v_3	v_4
Initial value	0 A	0 A	50 V	50 V	150 V	150 V

Waves of the proposed model are in good coincidence with the circuit simulation, which verifies its high accuracy in both the steady and dynamic large-signal processes.

2) Small-Signal Model Performance: The accuracy of the large-signal model can be presented more clearly using a system frequency-response analysis based on the small-signal model. This analysis is under the boost mode since the control methods in a latter section are under the boost mode. $V_b = 40$ V,$V_s = 0$ V, $U_m = 100$ V, and $U_o = 400$ V. $R_o = 533\ \Omega$/267 Ω/160 Ω, which means the converter works under 30%, 60%, and 100% rated power, respectively. Two Bode diagrams describing the responses of $\mathrm{d}\phi_1$ to $\mathrm{d}U_o$ and $\mathrm{d}\phi_2$ to $\mathrm{d}U_m$ are shown in Figs. 8 and 9, respectively. The figures reveal high coincidence of the proposed model with the circuit simulation in the whole frequency range. Especially in Fig. 8, the highly coincident magnitude peak near the resonant frequency is critical in system analysis and control design, since this peak greatly influence the stability

$$\begin{cases} i_{Lr}^{\phi_1} = i_{Lr0} + i_{LrFl}^{\phi_1},\ i_{Lr}^{\phi_2} = i_{Lr0} + i_{LrFl}^{\phi_2},\ i_{Lr}^{\phi_1+\phi_2} = i_{Lr0} \\ \qquad + i_{LrFl}^{\phi_1+\phi_2},\ i_{Lr}^{2\pi} = i_{Lr0} + i_{LrFl}^{2\pi} \\ i_{Lr\mathrm{AV}} = \frac{1}{2}(w_0(i_{Lr}^0 + i_{Lr}^{\phi_1}) + w_1(i_{Lr}^{\phi_1} + i_{Lr}^{\phi_2}) \\ \qquad + w_2(i_{Lr}^{\phi_2} + i_{Lr}^{\phi_1+\phi_2}) + w_3(i_{Lr}^{\phi_1+\phi_2} + i_{Lr}^{2\pi})) \end{cases} \quad (23)$$

E. Comparison with Existing Modeling Methods

To compare the existing methods and the proposed modeling method, based on two methods (a zero-average-current model and an average-current-state model) in [15] and [23], two pairs of the large- and small-signal models of the converter are established in MATLAB/Simulink. Parameters are the same as the proposed models.

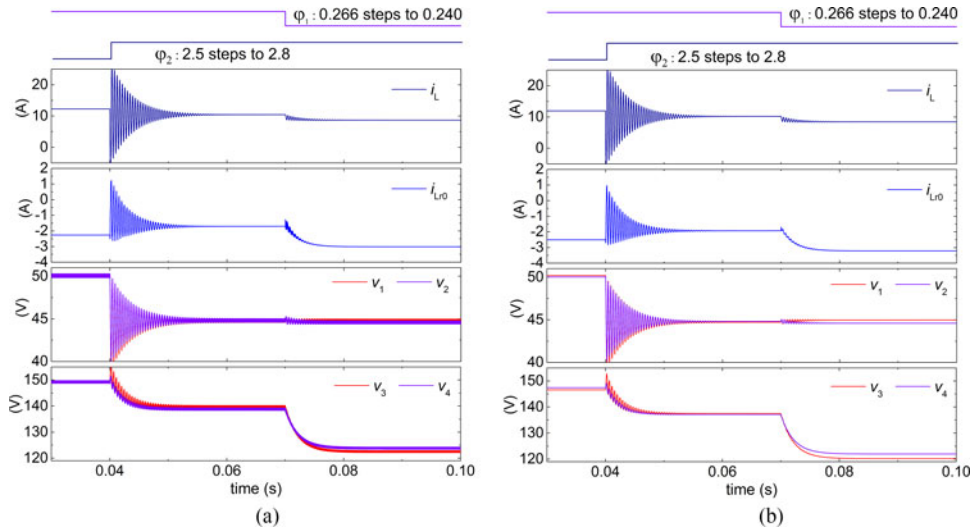

Fig. 6. Step response in boost mode: (a) circuit simulation and (b) proposed modeling.

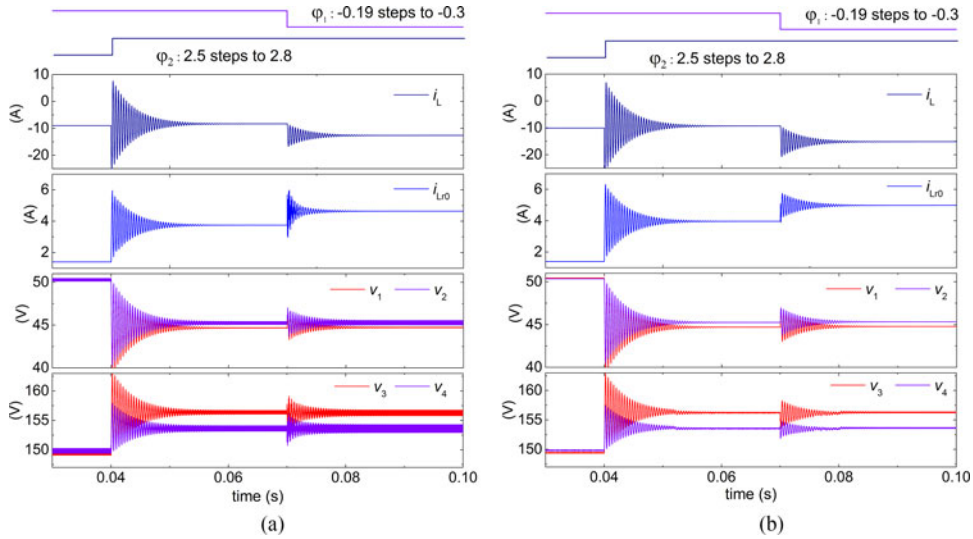

Fig. 7. Step response in buck mode: (a) circuit simulation and (b) proposed of modeling.

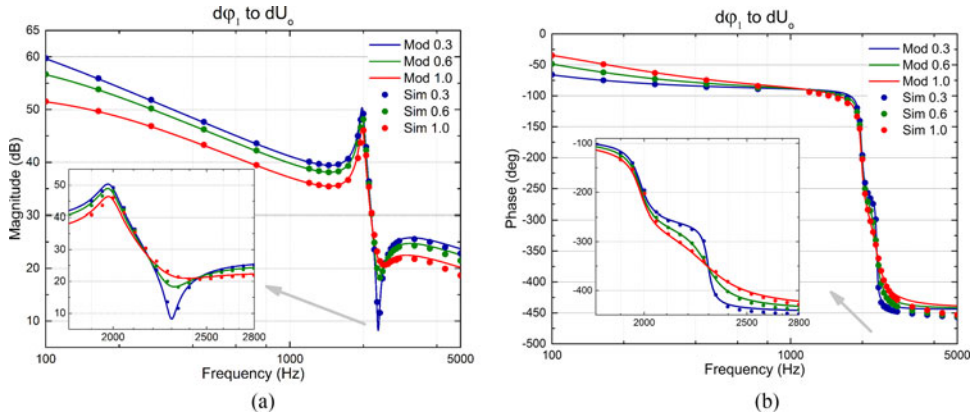

Fig. 8. Model frequency response and simulation spectrum for (a) magnitude $\mathrm{d}\varphi_1$–$\mathrm{d}U_\mathrm{o}$ and (b) phase $\mathrm{d}\varphi_1$–$\mathrm{d}U_\mathrm{o}$.

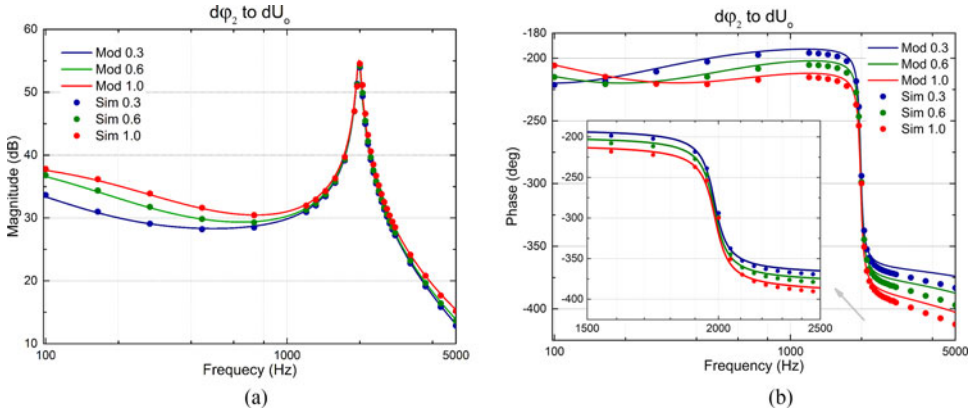

Fig. 9. Model frequency response and simulation spectrum for (a) magnitude $\mathrm{d}\varphi_2$–$\mathrm{d}U_\mathrm{o}$ and (b) phase $\mathrm{d}\varphi_2$–$\mathrm{d}U_\mathrm{o}$.

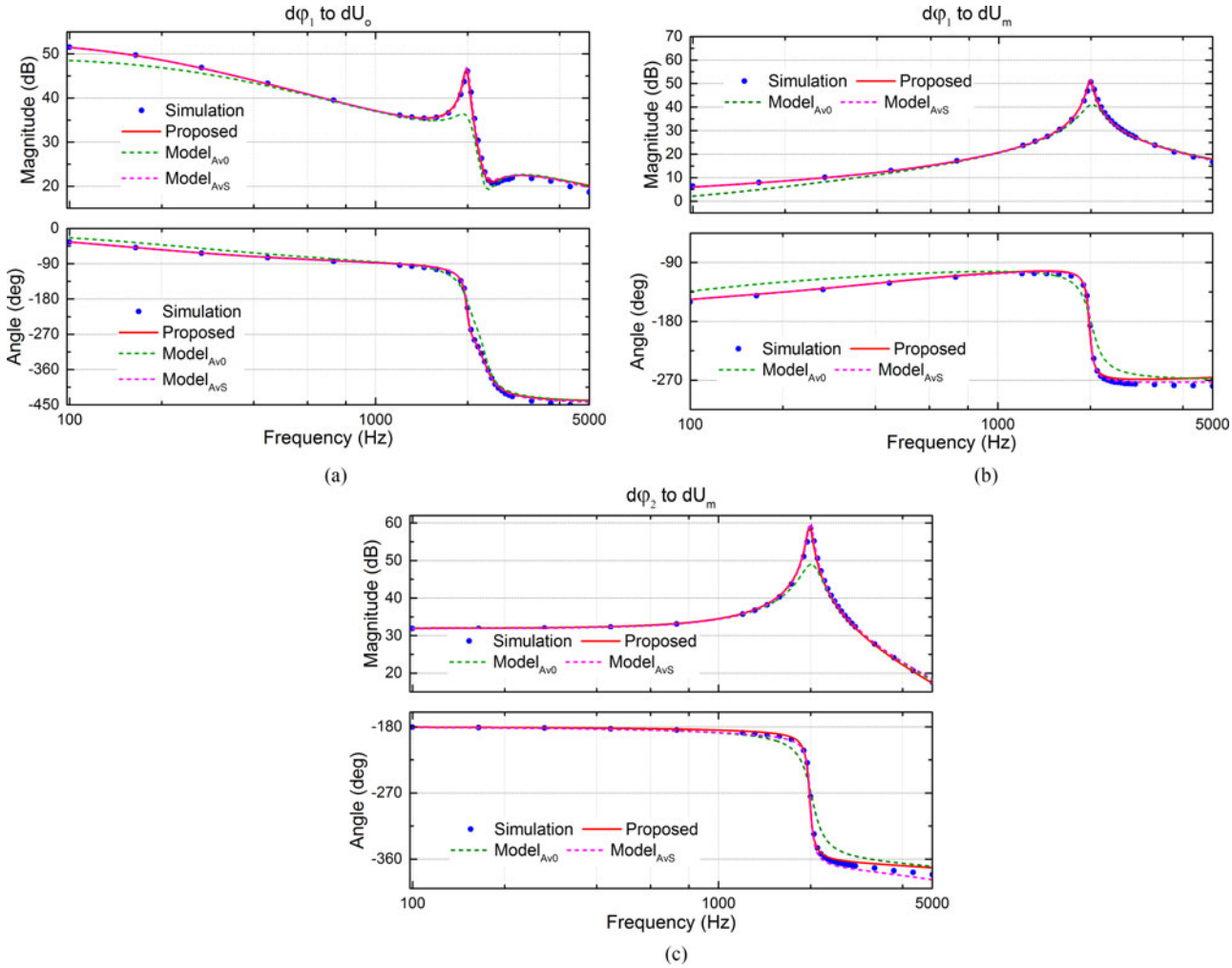

Fig. 10. Model frequency response comparison: (a) $\mathrm{d}\varphi_1$–$\mathrm{d}U_\mathrm{o}$, (b) $\mathrm{d}\varphi_1$–$\mathrm{d}U_\mathrm{m}$, and (c) $\mathrm{d}\varphi_2$–$\mathrm{d}U_\mathrm{m}$.

1) Zero-Average-Current Reduced Order Modeling: A brief introduction to the zero-average-current reduced order modeling method [15] is merited. In [15], ϕ_2 is limited to a constant π. To compare with the proposed method, ϕ_2 is liberated to a variable in this paper. This method assumes that the PWM cycle average of the series inductance current is zero: $i_{Lr\mathrm{AV}} = 0$. As in (23), the $i_{Lr\mathrm{AV}}$ can be expressed by five values i_{Lr}^{0}, $i_{Lr}^{\phi_1}$, $i_{Lr}^{\phi_2}$, $i_{Lr}^{\phi_1+\phi_2}$, and $i_{Lr}^{2\pi}$, which are the values of i_{Lr} when $\omega t =$

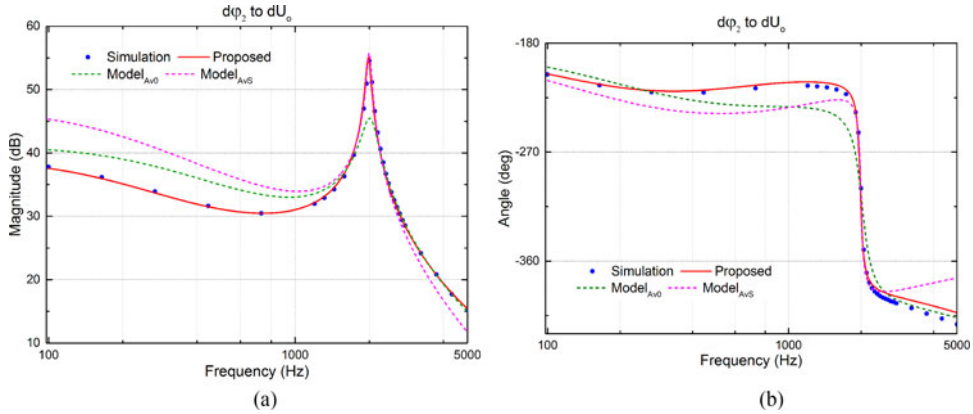

Fig. 11. Model frequency response comparison on $\mathrm{d}\varphi_2$–$\mathrm{d}U_\mathrm{o}$: (a) magnitude and (b) phase.

TABLE III
MODEL COMPARISON

Model type	Model	Coincidence compared with circuit simulation			algebraic degree
		Steady state	Dynamic state		
Large signal	Zero-average	medium	medium		3
	Average-state	high	very high		3
	Proposed	very high	very high		2
Model type	**Model**	**Low frequency**	**Resonant frequency**	**Very high frequency**	**algebraic degree**
Small signal	Zero-average	medium	low	high	3
	Average-state	high	very high	medium	3
	Proposed	very high	very high	high	2

0, ϕ_1, ϕ_2, $\phi_1+\phi_2$, 2π, respectively. Since i^0_{LrFl}, $i^{\phi_1}_{LrFl}$, $i^{\phi_2}_{LrFl}$, $i^{\phi_1+\phi_2}_{LrFl}$, $i^{2\pi}_{LrFl}$ are derived in (9) with ϕ_1, ϕ_2 and $[v]$, i_{Lr0} can be derived from (23) with $i_{Lr\mathrm{AV}}=0$. Then, i^0_{Lr}, $i^{\phi_1}_{Lr}$, $i^{\phi_2}_{Lr}$, $i^{\phi_1+\phi_2}_{Lr}$, $i^{2\pi}_{Lr}$ can be obtained and are used to calculate the change rates of the capacitor voltages. Finally, the whole five-order large- and small-signal models are built.

The main shortcoming of this method is that: v_1-v_2, v_3-v_4 are two constants determined by initial values. Since it always holds two equations $\dot{v}_1=\dot{v}_2$, $\dot{v}_3=\dot{v}_4$ due to its symmetry of state-space equations. This symmetry comes from the zero-average-current assumption $i_{Lr\mathrm{AV}}=0$. However, when ϕ_1 or ϕ_2 changes, v_1-v_2 and v_3-v_4 should varies with it as shown in Figs. 8 and 9. This problem causes obvious errors in the steady state, and even makes inequality between the input and output power. Dynamic performance is also influenced. Its frequency responses of small-signal models are shown in Figs. 10 and 11, for comparison with the average-current-state model and the proposed method.

2) Average-Current-State Full-Order Modeling Method: Equation (23) has also been used in the average-current-state full-order modeling from the method in [23], but it sets $i_{Lr\mathrm{AV}}$ as a state variable. This is more accurate than the zero-average-current method. There are two variables i_{Lr0}, $i_{Lr\mathrm{AV}}$ that determine i_{Lr}. During a PWM cycle $\mathrm{cycle}^{[n]}$, if given one of i_{Lr0} and $i_{Lr\mathrm{AV}}$, the other is derived. Since $i_{Lr\mathrm{AV}}$ is a state variable, $i_{Lr\mathrm{AV}}$ should be obtained from its initial value and the state equation $\dot{i}_{Lr\mathrm{AV}}$, then i_{Lr0} is derived. However, $\dot{i}_{Lr\mathrm{AV}}$ is hard to be derived according to the idea of that method. Generally, before deriving the $i_{Lr\mathrm{AV}}$ of next PWM cycle $\mathrm{cycle}^{[n+1]}$, the values i^0_{Lr}, $i^{\phi_1}_{Lr}$, $i^{\phi_2}_{Lr}$, $i^{\phi_1+\phi_2}_{Lr}$, $i^{2\pi}_{Lr}$ of $\mathrm{cycle}^{[n+1]}$ must have been acquired, which is equivalent to that i_{Lr0} of $\mathrm{cycle}^{[n+1]}$ must have been acquired. But with that method, i_{Lr0} of $\mathrm{cycle}^{[n+1]}$ has to be derived with $i_{Lr\mathrm{AV}}$ of $\mathrm{cycle}^{[n+1]}$. This contradiction is inherent. So in [23], an approximate substitute is made to deal with this problem, that the following equation is used as the state equation of $i_{Lr\mathrm{AV}}$. But in fact, it is the state equation of i_{Lr0} as shown in (10). So (24) means an approximation between two concepts

$$\dot{i}_{Lr\mathrm{AV}}=\frac{\phi_2 n}{2\pi L_r}v_1-\frac{(2\pi-\phi_2)n}{2\pi L_r}v_2-\frac{\phi_2}{2\pi L_r}v_3+\frac{2\pi-\phi_2}{2\pi L_r}v_4. \tag{24}$$

Its waves of large-signal model show good results. They are not given in this paper because the frequency responses of small-signal models in Figs. 10 and 11 show the comparison with

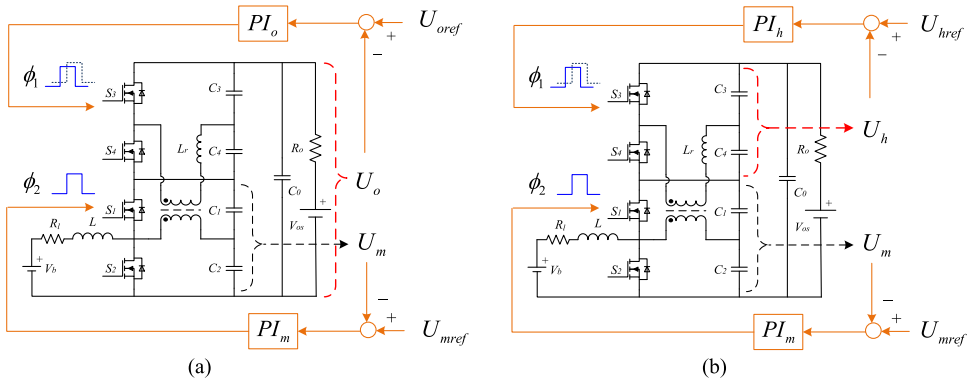

Fig. 12. Control diagrams: (a) coupled control strategy and (b) decoupled control strategy.

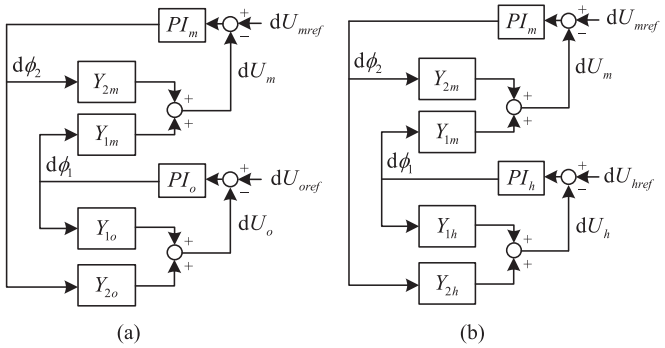

Fig. 13. Small-signal model diagrams of (a) coupled and (b) decoupled control strategy.

TABLE IV
PI PARAMETERS

Coupled control strategy	$\boldsymbol{PI_m}$ $\boldsymbol{K}_{pm}$ 1×10^{-4}	$\boldsymbol{K}_{im}$ 1	$\boldsymbol{PI_o}$ $\boldsymbol{K}_{po}$ $5\times10^{-3}\times K$	$\boldsymbol{K}_{io}$ $1.2765\times K$	$\boldsymbol{K}$ 1.9681
Decoupled control strategy	$\boldsymbol{PI_m}$ $\boldsymbol{K}_{pm}$ 1×10^{-4}	$\boldsymbol{K}_{im}$ 1	$\boldsymbol{PI_h}$ $\boldsymbol{K}_{ph}$ $5\times10^{-3}\times K$	$\boldsymbol{K}_{ih}$ $1.2765\times K$	$\boldsymbol{K}$ 2.2294

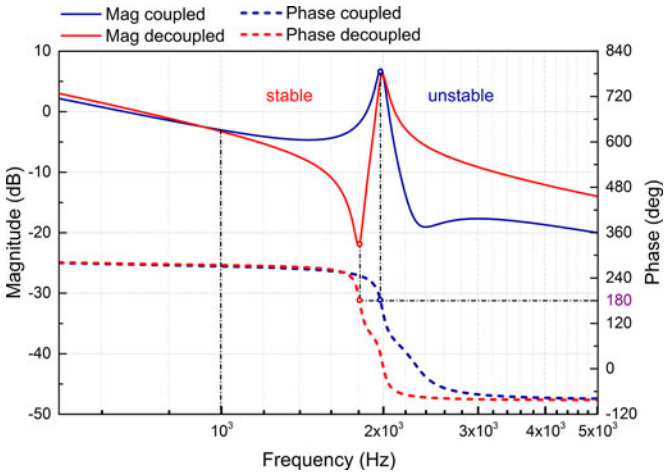

Fig. 14. Bode diagram of G_{dUoref} and G_{dUhref}.

the zero-average-current model and the proposed model more clearly.

3) Frequency Response of Small-Signal Models: Fig. 10 presents the frequency responses of three small signal models (the zero-average-current model $\mathrm{Model_{Av0}}$, the average-current-state model $\mathrm{Model_{AvS}}$, and the proposed model) and the spectrum of circuit simulation. The frequency responses are of $\mathrm{d}\phi_1$ to $\mathrm{d}U_o$ and $\mathrm{d}\phi_2$ to $\mathrm{d}U_o$. The steady state is under the boost mode at the following conditions: $V_b = 40$ V,$V_s = 0$ V, $U_m = 100$ V, and $U_o = 400$ V. $R_o = 160\ \Omega$.

For the zero-average-current model, its frequency responses suffer large deviation near the resonant frequency and a small deviation in low-frequency area as in Fig. 10. The magnitude peak on the resonant frequency is critical for the system stability analysis. Such deviation makes the zero-average-current model fail to reveal the peak.

For the average-current-state model, in most range, its frequency responses are highly coincident with the circuit simulation as shown in Fig. 10. However, in Fig. 11 of the response on $\mathrm{d}\phi_2$ to $\mathrm{d}U_o$, it fails to keep high coincidence with the circuit simulation, some large phase deviation appears. This can be a verification that (24) impairs the model accuracy, since the control variable in (24) is ϕ_2.

4) Summary on Comparison: Comparison of these models presented in the preceding subsection is summarized in Table III. More $*$ means higher coincidence with the circuit simulation.

By the zero-average-current modeling method, $i_{Lr\mathrm{AV}}$ is forced to be zero. Hence, the model order is reduced. But its large-signal model suffers a large deviation in dynamic and steady states. Its small-signal model shows its relatively poor accuracy in medium- and low-frequency range, especially near the resonant frequency.

The average-current-state modeling has made an important improvement on considering the change of $i_{Lr\mathrm{AV}}$ and utilizing it as a state variable, but has difficulty to obtain its state equation $\dot{i}_{Lr\mathrm{AV}}$ accurately. Steady and dynamic waves of large-signal model match the circuit simulation well.

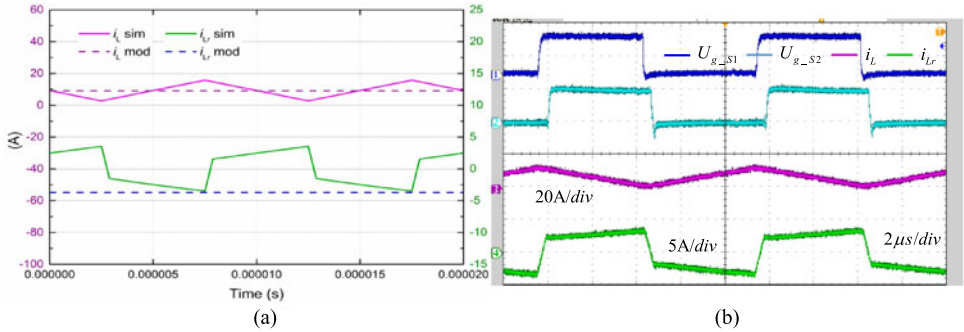

Fig. 15. Cycle waves in initial steady state: (a) simulation and model waves and (b) experimental waves.

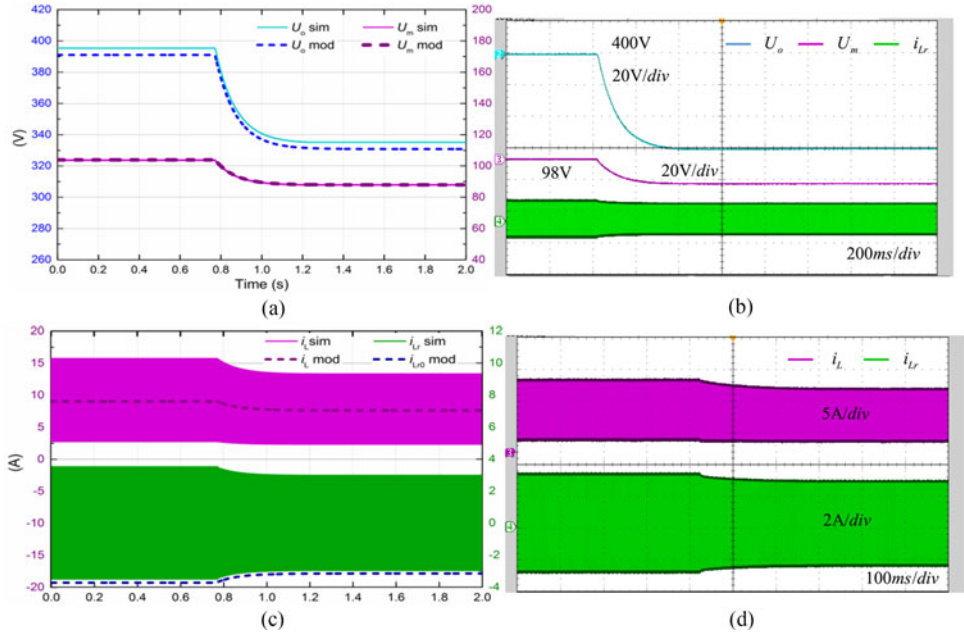

Fig. 16. Voltage and current waves with V_b step in simulation, model, and experiment: U_m and U_o in (a) simulation and model and (b) experiment; i_L and i_{Lr} in (c) simulation and model and (d) i_L in experiment.

The frequency responses within most of the frequency range match the circuit simulation well, except that of d φ_2 to d U_o.

In the proposed modeling method, the change of $i_{Lr\mathrm{AV}}$ has also been considered, and the idea that directly dividing i_{Lr} into i_{Lr0} and i_{LrFl} avoids the problem [mentioned above (24)] of deriving state equation $\dot{i}_{Lr\mathrm{AV}}$. Both its large- and small-signal models feature much better steady and dynamic coincidence with the circuit simulation. Expressions of ϕ_1 and ϕ_2 in state equations are square [shown in (14)], while those in zero-average-current and average-current-state models are cubic (presented in [23]). This lower algebraic degree benefits for the decrease of the model complexity. Due to its high dynamic and steady accuracy and low complexity, the proposed modeling method provides a better theoretical analysis and fast simulation tool for the transient process and the control design of converters with DAB units, especially with DHB units.

IV. Decoupled Control Strategy

The coupling and stacking scheme of VM-SDCT BDCs may adversely affect control stability. The studied converter BB-SDHB BDC as an example of this family and with the reuse of switches suffers even more severely from that. Thus, effective, simple, and more stable control should be applied. In this paper, a "decoupled PI control strategy" is proposed for VM-SDCT BDCs. That is: Under boost mode, supplying R_o with $V_s = 0$ V, one PI controller is used to regulate U_m by VM unit, and another PI controller to regulate U_h by SDCT unit. While the conventional "coupled control strategy" is: one PI controller is used to regulate U_m by VM unit, and another PI controller to regulate U_o by SDCT unit. Fig. 12 shows the two control strategies when they are applied to BB-SDHB BDC. They are analyzed based on the proposed models, which can also be considered as an application example of the modeling method.

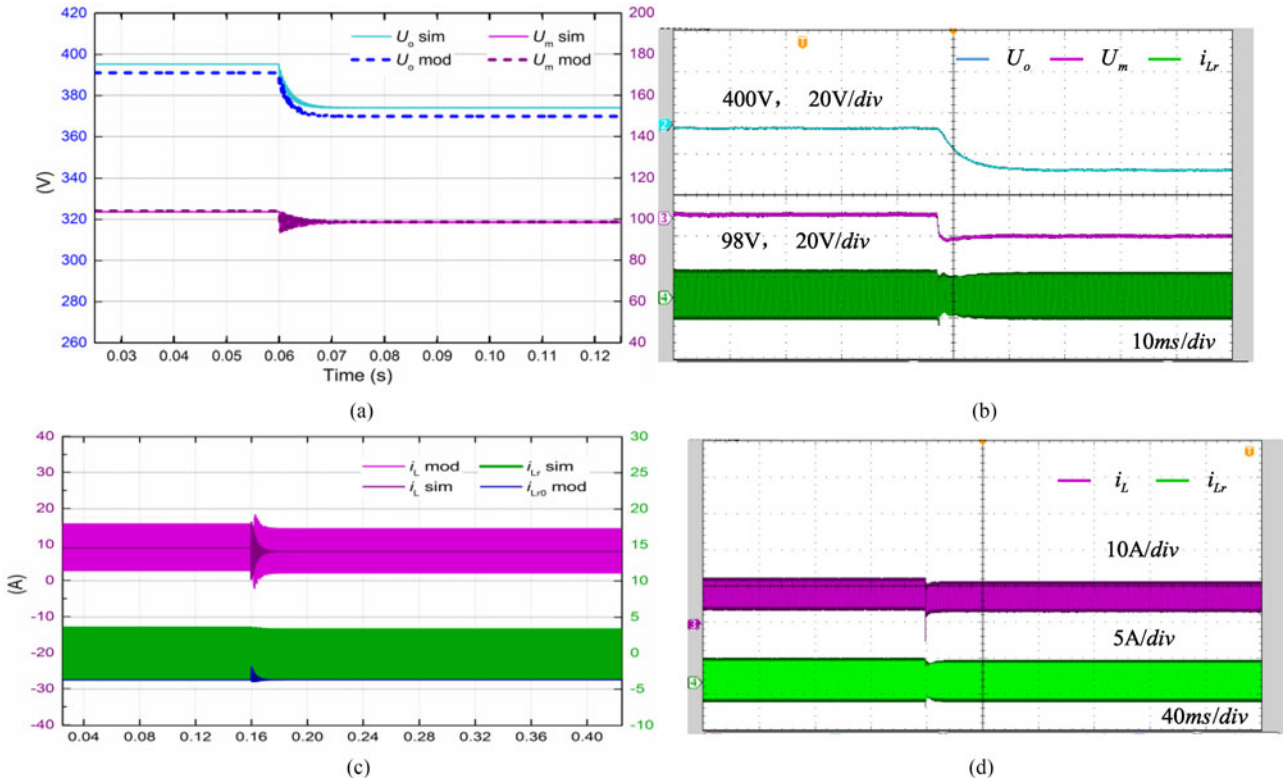

Fig. 17. Voltage and current waves with ϕ_2 step in simulation, model, and experiment: U_m and U_o in (a) simulation and model and (b) in experiment; i_L and i_{Lr} in (c) simulation and model and (d) in experiment.

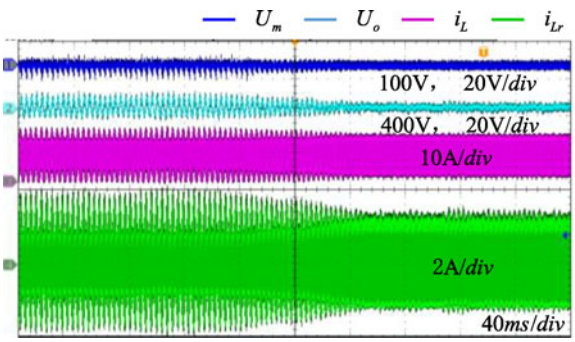

Fig. 18. Oscillations eliminated by switching to decoupled control strategy.

A. Coupling in Conventional Control

The primary and secondary voltage must match the transformer ratio to reduce reactive circulation. Under boost mode, supplying R_o with $V_s = 0$ V, achieving voltage matching means to control the intermediate voltage U_m and the secondary side voltage U_h. For the load, the output voltage U_o is the most important variable, and, if U_m and U_o are stabilized at their references, so is U_h. Along this line, two PI controllers PI_m, PI_o that control U_m and U_o can be easily applied. U_m is regulated by ϕ_2 with the buck–boost unit, and U_o is regulated by ϕ_1, which determines the power delivered by the transformer between $C_{1\sim2}$ (U_m) and $C_{3\sim4}$ (U_h), as shown in Fig. 12(a). However, due to strong coupling, this coupled control strategy causes oscillation relatively easily. For instance, increasing ϕ_1 helps transfer more power from the primary side to the secondary side, and makes U_h rise while making U_m fall slightly. Hence, U_h follows ϕ_1 to increase, while U_m does not, which means a part of $U_o = U_m + U_h$ varies with ϕ_1 in the inverse direction.

B. Proposed Decoupled Control Strategy

On the basis of the aforesaid analysis, a solution such as that shown in Fig. 12(b) can be easily derived; that is, two PI controllers PI_m, PI_h that control U_m and U_h, respectively. Similarly, if U_m and U_h are stabilized at their references, so is U_o. By this means, ϕ_1 and ϕ_2 are used to regulate the voltages that they directly affect. Such specialization upgrades stability, though this decoupled control strategy makes U_o indirectly controlled, and, the speed of response is determined by the slower one of the two PI loops (usually the loop of U_m). It costs no more in terms of calculation and complexity compared with the coupled control strategy. For the studied converter, some quantitative analyses of performance under the two controls are now presented.

C. Frequency Response Comparison

The two control blocks in the frequency domain based on the small-signal modeling are depicted in Fig. 13, where Y_{pq}

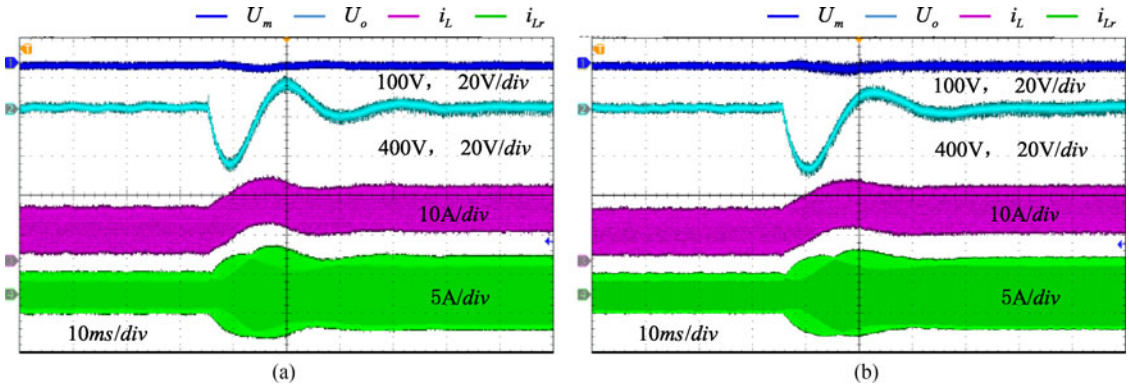

Fig. 19. Load steps from 40% to 70%: (a) coupled control strategy and (b) decoupled control strategy.

represents the transfer functions of $\mathrm{d}U_m$, $\mathrm{d}U_o$, and $\mathrm{d}U_h$ about $\mathrm{d}\phi_1$ and $\mathrm{d}\phi_2$.

Considering the superposition principle, when $\mathrm{d}U_{\mathrm{mref}}$ is 0, the open-loop transfer functions of $\mathrm{d}U_{\mathrm{oref}}$ and $\mathrm{d}U_{\mathrm{href}}$ are

$$G_{\mathrm{dUoref}}(s) = PI_{\mathrm{o}} \frac{(1 + Y_{2m} PI_m) Y_{1o} - Y_{1m} PI_m Y_{2o}}{1 + Y_{2m} PI_m}, \quad (25)$$

$$G_{\mathrm{dUhref}}(s) = PI_h \frac{(1 + Y_{2m} PI_m) Y_{1h} - Y_{1m} PI_m Y_{2h}}{1 + Y_{2m} PI_m}. \quad (26)$$

The PI_m parameters are adjusted to proper values and fixed. PI_o and PI_h are set to parameters that eliminate the dominant pole of the open-loop transfer function and bring the crossing frequency to 1000 Hz. Steady working points are $V_b = 52\,\mathrm{V}, V_{os} = 0\,\mathrm{V}, R_o = 160\,\Omega$, $U_m = 100\,\mathrm{V}$, and $U_o = 400\,\mathrm{V}$. The converter system parameters are given in Table I. The PI parameters are given in Table IV, where K_{pm} and K_{im} are the proportional and integral coefficients of PI_m, similar for K_{po} and K_{io} of PI_o, K_{ph} and K_{ih} of PI_h. The systems' structural differences in terms of stability are shown in the Bode diagrams of G_{dUoref} and G_{dUhref} presented in Fig. 14.

As shown in Fig. 14, at the frequency of 180°, G_{dUoref} (coupled one) magnitude of the coupled control strategy appears a peak far higher than 0 dB, while G_{dUhref} (decoupled one) magnitude of the decoupled control strategy appears a valley far lower than 0 dB. Thus, the decoupled control strategy obtains a very large magnitude margin compared with the coupled control strategy, resulting in much higher stability.

V. Experimental Verification

Proposed large-signal modeling, switching circuit simulation, and experimental results are presented together to verify the proposed modeling technique and the performance of the decoupled control strategy. The experiments have been carried out on a 1-kW prototype. Most component parameters are listed in Table I, but some are different: $L_{\mathrm{m}} = 10\,\mathrm{mH}$; unknown but very small R_l; some electrolytic capacitors are in the prototype. The switching devices used in the prototype were model IPP075N15N3G for S_1, S_2 and model IXFH16N50P for S_3, S_4. Initial working conditions are as follows: $V_b = 52$ V, $V_s = 0$ V, $R_o = 326.1\,\Omega$, $\phi_2 = 3.1415$, and $\phi_1 = 0.2409$, respectively, which makes U_m and U_o close to their rated values (100 and 400 V). All working conditions are the same in the proposed model, circuit simulation, and experiment.

A. Modeling Verification

The model results were compared with those from circuit simulation and experiment under transient processing with variation of input voltage V_b and duty cycle phase ϕ_2.

1) Steady State Before Step: Detailed cycle waves of the model, simulation, and experiment in the initial steady state are shown in Fig. 15. i_{Lr0} in the model is very close to its value in the simulation at sampling time. All waves match each other well.

2) V_{b} Variation: The V_b steps from 52 to 44 V . Since the input dc voltage source cannot change in a stepwise way, the V_{b} stepping takes a relatively long time. The waves of U_o, U_m, i_L, and i_{Lr} are shown in Fig. 16, where simulation, modeling, and experimental results are coincident with each other.

3) Duty-Cycle Stepping: The duty cycle $\phi_2/2\pi$ steps from 0.5000 to 0.5267. As in Fig. 17, the waves in the model and circuit simulation show much higher-frequency transients than in experiment, due to the electrolytic capacitors and other nonideal characteristics of the prototype. Simulation, modeling, and experiment are in agreement with each other.

B. Coupled Control Strategy and the Proposed Decoupled Control Strategy

Coupled and decoupled control strategies are compared under dynamic and steady situations to test their characteristics.

1) Stability Verification: At the beginning, the coupled control strategy causes oscillations as depicted in Fig. 18 under certain PI parameters. After directly switching to the decoupled control strategy under the same PI parameters (which means a similar crossing frequency, based on details provided in Section IV), the oscillations disappears. The waves verified the higher stability of the decoupled control strategy method.

2) Load Step Response: Smaller and the same PI parameters are set to keep the system stable under both control methods; the parameters also comprise two controls under the similar crossing frequency based on the discussion in Section IV. Test working conditions are load stepped from 40% to 70%. Coupled and decoupled control strategy show nearly the same response from inspection of Fig. 19, but the much higher stability of the decoupled control strategy facilitates adjustment of PI parameters for better response.

VI. Conclusion

This paper focuses on developing an extended, continuous, full order, state-space averaging modeling method. The proposed modeling method is for converters with phase shift plus duty cycle control. A converter BB-SDHB BDC is modeled by the proposed modeling method. Both nonlinear large-signal model and linear small-signal model are established. These two mathematic models highly coincide with switching circuit simulation in both steady and dynamic states. Experimental results validate the correctness and accuracy of the proposed modeling method. Simulation comparison with two existing advanced modeling methods also shows the higher accuracy of the proposed one. Due to its high dynamic and steady accuracy and low complexity, the proposed modeling method provides a better theoretical analysis and fast simulation tool for transient process and control design of converters with DAB units, especially with DHB units.

A decoupled control strategy is also proposed to achieve a better control stability of the VM-SDCT BDCs. For the BB-SDHB BDC, the effectiveness of this control strategy is analyzed based on the proposed model, which is also an application of this modeling method. Experimental results also show its improved stability.

VII. Appendix

The completed large-signal model are presented in

$$\begin{bmatrix} \dot{i}_L \\ \dot{i}_{Lr0} \\ \dot{v}_1 \\ \dot{v}_2 \\ \dot{v}_3 \\ \dot{v}_4 \end{bmatrix} = \begin{bmatrix} -\dfrac{R_l}{L} & 0 & [H_{i_L\_v}] \\ 0 & 0 & [H_{i_{Lr0}\_v}] \\ [H_{v\_i_L}] & [H_{v\_i_{Lr0}}] & [H_{v\_v}] \end{bmatrix} \begin{bmatrix} i_L \\ i_{Lr0} \\ v_1 \\ v_2 \\ v_3 \\ v_4 \end{bmatrix} + \begin{bmatrix} \dfrac{1}{L} & 0 \\ 0 & 0 \\ [0] & \dfrac{[M_{C\_Ro}]}{R_0} \end{bmatrix} \begin{bmatrix} V_b \\ V_{os} \end{bmatrix} \tag{27}$$

where see equation shown at the bottom of this page, as well as the equation shown at the top of the next page.

$$C_{iN} = 1/\sum_{j\neq i}^{M=0\sim4} \frac{1}{C_j}, C_{Lp} = \frac{C_1C_2}{C_1+C_2}, C_{Ls} = \frac{C_3C_4C_0}{C_3C_4+C_4C_0+C_3C_0},$$

$$\frac{[M_{C\_Ro}]}{R_o} = \frac{C_{0N}}{R_o(C_{0N}+C_0)} \begin{bmatrix} \frac{1}{C_1} & \frac{1}{C_2} & \frac{1}{C_3} & \frac{1}{C_4} \end{bmatrix}^{\mathrm{T}}$$

$$H_{i_L\_v} = \begin{bmatrix} -\frac{\phi_2}{2\pi L} & -\frac{\phi_2}{2\pi L} & 0 & 0 \end{bmatrix},$$

$$H_{i_{Lr0}\_v} = \begin{bmatrix} \frac{\phi_2 n}{2\pi L_r} & -\frac{(2\pi-\phi_2)n}{2\pi L_r} & -\frac{\phi_2}{2\pi L_r} & \frac{2\pi-\phi_2}{2\pi L_r} \end{bmatrix}$$

$$H_{v\_i_L} = \frac{\phi_2}{2\pi(C_{Lp}+C_{Ls})} \begin{bmatrix} C_{Lp}/C_1 \\ C_{Lp}/C_2 \\ -C_{Ls}/C_3 \\ -C_{Ls}/C_4 \end{bmatrix},$$

$$H_{v\_i_{Lr0}} = \frac{1}{2\pi} \begin{bmatrix} \frac{-n}{C_{1n}+C_1} & -\frac{nC_{2n}}{C_1(C_{2n}+C_2)} & -\frac{C_{3n}}{C_1(C_{3n}+C_3)} & \frac{C_{4n}}{C_1(C_{4n}+C_4)} \\ \frac{nC_{1n}}{C_2(C_{1n}+C_1)} & \frac{n}{C_{2n}+C_2} & -\frac{C_{3n}}{C_2(C_{3n}+C_3)} & \frac{C_{4n}}{C_2(C_{4n}+C_4)} \\ \frac{nC_{1n}}{C_3(C_{1n}+C_1)} & -\frac{nC_{2n}}{C_3(C_{2n}+C_2)} & \frac{1}{C_{3n}+C_3} & \frac{C_{4n}}{C_3(C_{4n}+C_4)} \\ \frac{nC_{1n}}{C_4(C_{1n}+C_1)} & -\frac{nC_{2n}}{C_4(C_{2n}+C_2)} & -\frac{C_{3n}}{C_4(C_{3n}+C_3)} & \frac{-1}{C_{4n}+C_4} \end{bmatrix} \begin{bmatrix} \phi_2 \\ (2\pi-\phi_2) \\ \phi_2 \\ (2\pi-\phi_2) \end{bmatrix}$$

$$H_{v\_v} = \frac{T_s}{8\pi^2 L_r} \begin{bmatrix} \frac{-n}{C_{1N}+C_1} & -\frac{nC_{2N}}{C_1(C_{2N}+C_2)} & -\frac{C_{3N}}{C_1(C_{3N}+C_3)} & \frac{C_{4N}}{C_1(C_{4N}+C_4)} \\ \frac{nC_{1N}}{C_2(C_{1N}+C_1)} & \frac{n}{C_{2N}+C_2} & -\frac{C_{3N}}{C_2(C_{3N}+C_3)} & \frac{C_{4N}}{C_2(C_{4N}+C_4)} \\ \frac{nC_{1N}}{C_3(C_{1N}+C_1)} & -\frac{nC_{2N}}{C_3(C_{2N}+C_2)} & \frac{1}{C_{3N}+C_3} & \frac{C_{4N}}{C_3(C_{4N}+C_4)} \\ \frac{nC_{1N}}{C_4(C_{1N}+C_1)} & -\frac{nC_{2N}}{C_4(C_{2N}+C_2)} & -\frac{C_{3N}}{C_4(C_{3N}+C_3)} & \frac{-1}{C_{4N}+C_4} \end{bmatrix}$$

$$\times \begin{bmatrix} n\phi_2^2 & 0 & -(\phi_2-\phi_1)^2 & -\phi_1^2+2\phi_1\phi_2 \\ 2n\phi_2(2\pi-\phi_2) & -n(2\pi-\phi_2)^2 & \phi_1^2+2\phi_2^2-4\pi\phi_2 & \phi_1^2+(2\pi-\phi_2)^2 \\ n(-\phi_1^2+2\phi_1\phi_2+\phi_2^2) & -n\phi_1^2 & -\phi_2^2 & 2\phi_1\phi_2 \\ n(\phi_1^2+2\phi_2(2\pi-\phi_1-\phi_2)) & n(\phi_1^2-(2\pi-\phi_2)^2) & -2\phi_2(2\pi-\phi_1-\phi_2) & (2\pi-\phi_2)^2 \end{bmatrix}$$

$$-\frac{C_{0N}}{R_o(C_{0N}+C_0)} \begin{bmatrix} \frac{1}{C_1} & \frac{1}{C_1} & \frac{1}{C_1} & \frac{1}{C_1} \\ \frac{1}{C_2} & \frac{1}{C_2} & \frac{1}{C_2} & \frac{1}{C_2} \\ \frac{1}{C_3} & \frac{1}{C_3} & \frac{1}{C_3} & \frac{1}{C_3} \\ \frac{1}{C_4} & \frac{1}{C_4} & \frac{1}{C_4} & \frac{1}{C_4} \end{bmatrix}.$$

REFERENCES

[1] T.-J. Liang and J.-H. Lee, "Novel high-conversion-ratio high-efficiency isolated bidirectional DC–DC converter," *IEEE Trans. Ind. Electron.*, vol. 62, no. 7, pp. 4492–4503, Jul. 2015

[2] H. Wu, K. Sun, L. Chen, L. Zhu, and Y. Xing, "High step-up/step-down soft-switching bidirectional DC–DC converter with coupled-inductor and voltage matching control for energy storage systems," *IEEE Trans. Ind. Electron.*, vol. 63, no. 5, pp. 2892–2903, May 2016.

[3] K. Filsoof and P. W. Lehn, "A bidirectional modular multilevel DC–DC converter of triangular structure," *IEEE Trans Power Electron.,* vol. 30, no. 1, pp. 54–64, Jan. 2015.

[4] D. Cao and F. Z. Peng, "Zero-current-switching multilevel modular switched-capacitor DC-DC converter," in *Proc. IEEE Energy Conver. Congr. Expo.*, San Jose, CA, USA, 2009, pp. 3516–3522.

[5] S. Xiong, S. C. Tan, and S. C. Wong, "Analysis and design of a high-voltage-gain hybrid switched-capacitor buck converter," *IEEE Trans. Circuits Syst. I: Regular Pap.*, vol. 59, no. 5, pp. 1132–1141, May 2012.

[6] T. J. Liang, S. M. Chen, L. S. Yang, J. F. Chen, and A. Ioinovici, "Ultra-large gain step-up switched-capacitor DC-DC converter with coupled inductance for alternative sources of energy," *IEEE Trans. Circuits Syst. I: Reg. Papers*, vol. 59, no. 4, pp. 864–874, Apr. 2012.

[7] W. Qian *et al.*, "A switched-capacitor DC–DC converter with high voltage gain and reduced component rating and count," *IEEE Trans. Ind. Appl.*, vol. 48, no. 4, pp. 1397–1406, Jul./Aug. 2012.

[8] P. Das, S. A. Mousavi, and G. Moschopoulos, "Analysis and design of a nonisolated bidirectional ZVS-PWM DC–DC converter with coupled inductances," *IEEE Trans. Power Electron.,* vol. 25, no. 10, pp. 2630–2641, Oct. 2010.

[9] S. Park and S. Choi, "Soft-switched CCM boost converters with high voltage gain for high-power applications," *IEEE Trans. Power Electron.*, vol. 25, no. 5, pp. 1211–1217, May 2010.

[10] H. Wen, W. Xiao, and B. Su, "Nonactive power loss minimization in a bidirectional isolated DC–DC converter for distributed power systems," in *IEEE Trans. Ind. Electron.,* vol. 61, no. 12, pp. 6822–6831, Dec. 2014.

[11] H. Li, F. Z. Peng, and J. Lawler, "Modeling, simulation, and experimental verification of soft-switched bi-directional DC-DC converters," in *Proc. IEEE 16th Annu. Appl. Power Electron. Conf. Expo.*, 2001, vol. 2, pp. 736–742.

[12] H. Wu *et al.*, "High step-up/step-down non-isolated BDC with built-in DC-transformer for energy storage systems," *IET Power Electron.*, vol. 9, no. 13, pp. 2571–2579, Oct. 26, 2016.

[13] M. Kasper, D. Bortis, and J. W. Kolar, "Classification and comparative evaluation of PV panel-integrated DC–DC converter concepts," *IEEE Trans. Power Electron.*, vol. 29, no. 5, pp. 2511–2526, May 2014.

[14] R. Middlebrook and S. Cuk, "A general unified approach to modeling switching-converter power stages," in *Power IEEE Electron. Spec. Conf.*, June 8–10, 1976, pp. 18–34.

[15] H. Li and F. Z. Peng, "Modeling of a new ZVS bi-directional dc-dc converter," *IEEE Trans. Aerosp. Electron. Syst.*, vol. 40, no. 1, pp. 272–283, Jan. 2004.

[16] H. K. Krishnamurthy and R. Ayyanar, "Building block converter module for universal (AC-DC, DC-AC, DC-DC) fully modular power conversion architecture," in *Proc. IEEE Power Electron. Spec. Conf.*, Orlando, FL, USA, 2007, pp. 483–489.

[17] H. Bai, C. Mi, C. Wang, and S. Gargies, "The dynamic model and hybrid phase-shift control of a dual-active-bridge converter," in *Proc. 34th Annu. Conf. IEEE Ind. Electron.*, Orlando, FL, USA, 2008, pp. 2840–2845.

[18] L. Sun, D. Xu, M. Chen, and X. Zhu, "Dynamic model of PWM plus phase-shift (PPS) control bidirectional DC-DC converters," in *Proc. 40th IAS Annu. Meeting Conf. Rec. 2005 Ind. Appl. Conf.*, 2005, vol. 1, pp. 614–619.

[19] "Dynamic modeling of a PWM plus phase-shift (PPS) controlled active clamping boost to full bridge Bi-directional DC/DC converter," in *Proc. 37th IEEE Power Electron. Spec. Conf.*, Jeju, South Korea, 2006, pp. 1–6.

[20] C. Zhao, S. D. Round, and J. W. Kolar, "Full-order averaging modeling of zero-voltage-switching phase-shift bidirectional DC-DC converters," *IET Power Electron.*, vol. 3, no. 3, pp. 400–410, May 2010.

[21] H. Daneshpajooh, A. Bakhshai, and P. Jain, "Modified dual active bridge bidirectional DC-DC converter with optimal efficiency," in *Proc. 27th Annu. IEEE Appl. Power Electron. Conf. Expo.*, Orlando, FL, USA, 2012, pp. 1348–1354.

[22] A. A. Aboushady, K. H. Ahmed, S. J. Finney, and B. W. Williams, "Linearized large signal modeling, analysis, and control design of phase-controlled series-parallel resonant converters using state feedback," *IEEE Trans. Power Electron.*, vol. 28, no. 8, pp. 3896–3911, Aug. 2013.

[23] H. Daneshpajooh, S. A. Khajehoddin, P. Jain, and A. Bakhshai, "Modeling of the phase shift plus duty cycle controlled half bridge DC to DC converter," in *Proc. 35th Int. Telecommun. Energy Conf. 'Smart Power Efficiency'*, Oct. 13–17, 2013, pp. 1–6.

Haixu Shi (S'16) received the B.S. degree in electrical engineering from Tsinghua University, Beijing, China, in 2014, where since 2014, he has been working toward the Ph.D. degree in electrical engineering.

His current research interests include DC–DC converters, distributed generation, and microgrid applications.

Xi Xiao (M'07) was born in Hunan Province, China, in 1973. He received the B.E., M.E., and Ph.D. degrees from Saint Petersburg State Technical University, Saint Petersburg, Russia, in 1995, 1997, and 2000, respectively.

Since 2001, he has been in the Department of Electrical Engineering and Applied Electronic Technology, Tsinghua University, Beijing, China, where he is currently a Full Professor and the Vice Dean of the department. His main areas of research interest are permanent-magnet synchronous motor control, power electronics, and renewable energy.

Hongfei Wu (S'11–M'13) was born in Hebei Province, China, in 1985. He received the B.S. and Ph.D. degrees in electrical engineering and power electronics and power drives from Nanjing University of Aeronautics and Astronautics (NUAA), Nanjing, China, in 2008 and 2013, respectively. From June 2012 to July 2012, he was a gust Ph.D. student at the Institute of Energy Technology, Aalborg University, Aalborg, Denmark.

Since 2013, he has been in the Faculty of Electrical Engineering, NUAA, and is currently an Associate Professor in College of Automation Engineering, NUAA. He has authored and coauthored more than 100 peer-reviewed papers published in journals and conference proceedings. He is the holder of more than 20 Patents. His research interests are power converters and distributed power generation system.

Dr. Wu received the Outstanding Reviewer of *IEEE Transactions on Power Electronics* (2013). He also received the Changkong Scholar Award of NUAA in 2017.

Kai Sun (M'12–SM'6) received the B.E., M.E., and Ph.D. degrees in electrical engineering from Tsinghua University, Beijing, China, in 2000, 2002, and 2006, respectively.

He joined the Faculty of Electrical Engineering, Tsinghua University, in 2006, where he is currently an Associate Professor. From September 2009 to August 2010, he was a Visiting Scholar at the Department of Energy Technology, Aalborg University, Aalborg, Denmark. From January to August 2017, he was a Visiting Professor at the Department of Electrical and Computer Engineering, University of Alberta, Edmonton, AB, Canada. His current research interests include power electronics for renewable generation systems, microgrids, and energy internet.

Dr. Sun is a Member of Ithe IEEE Power Electronics Society Sustainable Energy Systems Technical Committee, a Member of the IEEE Power Electronics Society Power and Control Core Technologies Committee, a Member of the IEEE Industrial Electronics Society Renewable Energy Systems Technical Committee, and a member of Ithe EEE IAS Industrial Drive Committee Awards Sub-committee. He served as the TPC Vice Chair of IEEE ECCE2017 and IEEE ECCE-Asia2017. He is an Associate Editor for the *Journal of Power Electronics*. He received the Delta Young Scholar Award in 2013.